

**Numerical Study of Integrated Micro Ring Resonator**

**by**

**Dachuan Wu**

**A thesis submitted in partial fulfillment**

**of the requirements for the degree of**

**Master of Science in Engineering**

**(Mechanical Engineering)**

**in the University of Michigan-Dearborn**

**2017**

**Master's Thesis Committee:**

**Professor Ben Q. Li, Co-Chair**

**Associate Professor Yasha Yi, Co-Chair**

**Assistant Professor Gargi Ghosh**

**Assistant Professor Joe Fu-Jiou Lo**

## **ACKNOWLEDGEMENTS**

Here I want to express my most sincere gratitude to Professor Yasha Yi, my thesis advisor, for his kindness and patient help. Without his help, this thesis definitely cannot be completed.

Also, I want to show my appreciation to my colleague Mao Ye, for his help and company during the days at UM-Dearborn.

At last, thank all the people who ever gave me a hand during the research work in this two years.

## TABLE OF CONTENTS

|   |     |
|---|-----|
| ACKNOWLEDGEMENTS.....   | ii  |
| LIST OF FIGURES .....   | v   |
| ABSTRACT.....   | vii |
| Chapter I   |     |
| Introduction and Basic Theory of Integrated Ring Resonator .....        | 1   |
| 1.1 Introduction .....  | 1   |
| 1.2 Basic Theory.....   | 1   |
| Chapter II  |     |
| Particle position sensor based on integrated double ring resonator..... | 18  |
| 2.1 Basic design.....   | 18  |
| 2.2 Design based on Cascaded Ring Resonators.....                       | 25  |
| 2.3 Conclusion.....   | 31  |
| Chapter III   |     |
| Plasmonic hydrogen sensor based on integrated micro ring resonator..... | 32  |
| 3.1 Introduction .....  | 32  |
| 3.2 Basic model and simulation .....                                    | 34  |
| 3.2.1 Model and simulation results .....                                | 34  |
| 3.2.2 Investigation of the coverage proportion of Pd/Pt layer.....      | 37  |

|   |    |
|---|----|
| 3.2.3 Investigation of the width of Pd/Pt layer.....                                      | 41 |
| 3.3 Conclusion.....   | 44 |
| Chapter IV  |    |
| High-Contrast Subwavelength Grating Structure for Wideband Reflector at Visible Light.... | 45 |
| 4.1 Introduction of HCG structure .....   | 45 |
| 4.2 The attempt of wideband reflector at visible light range.....                         | 46 |
| Chapter V   |    |
| Introduction of Finite Difference Time Domain (FDTD) method in Electromagnetism.....      | 49 |
| 5.1 Introduction .....  | 49 |
| 5.2 Yee Lattice .....   | 51 |
| 5.3 Maxwell's equations and their finite difference form.....                             | 52 |
| CONCLUSION.....   | 60 |
| REFERENCES .....  | 61 |
| PUBLICATIONS .....  | 65 |

## LIST OF FIGURES

|  |    |
|--|----|
| Fig. 1.1 Illustration of Integrated Ring Resonator .....                               | 1  |
| Fig. 1.2 Illustration of Electromagnetic Wave .....                                    | 2  |
| Fig. 1.3 Illustration of Planar Waveguide .....  | 3  |
| Fig. 1.4 Illustration of Reflection.....   | 3  |
| Fig. 1.5 Illustration of Waveguide .....   | 5  |
| Fig. 1.6 Single Rectangle Waveguide .....  | 6  |
| Fig. 1.7 Double Rectangle Waveguides .....   | 7  |
| Fig. 1.8 Illustration of frustrated total internal reflection .....                    | 8  |
| Fig. 1.9 Ring Resonator consists of a ring and a slab waveguide.....                   | 9  |
| Fig. 1.10 Model of a single ring resonator with one waveguide.....                     | 10 |
| Fig. 1.11 Ring Resonator consists of a ring and two slab waveguide.....                | 13 |
| Fig. 1.12 Model of a basic add-drop single ring resonator filter .....                 | 14 |
| Fig. 1.13 Illustration of Full-Width at Half Maximum and Free Spectral Range.....      | 16 |
| Fig. 1.14 Transmission spectrum of the ring resonator.....                             | 17 |
| Fig. 2.1. Particle position sensor based on parallel double ring resonator.....        | 19 |
| Fig. 2.2. Output of the device .....   | 20 |
| Fig. 2.3. Comparison between the real output and $T_{11} * Tr_1$ .....                 | 21 |
| Fig. 2.4. Output of the device when a Si particle exists close to ring resonator ..... | 22 |
| Fig. 2.5. Output of the device when an Au particle exists close to ring resonator..... | 23 |

|  |    |
|--|----|
| Fig. 2.6. Output of the device when a Si particle exists close to racetrack resonator.....   | 24 |
| Fig. 2.7. Output of the device when an Au particle exists close to racetrack resonator .....   | 25 |
| Fig. 2.8. Particle position sensor based on cascaded double ring resonator .....   | 27 |
| Fig. 2.9. Output of the device .....   | 28 |
| Fig. 2.10. Output of the device when nine Si particles exist close to resonator .....  | 29 |
| Fig. 2.11. Output of the device when three Si particles exist close to resonator .....   | 31 |
| Fig. 3.1 Device model.....   | 35 |
| Fig. 3.2 Resonance wavelength shift and relative intensity change of the fully covered ring resonator hydrogen sensor with hydrogen concentration variation from 0~1%..... | 36 |
| Fig. 3.3 The comparison between Pd- and Pt- coated structures .....  | 38 |
| Fig. 3.4 Top view of the ring resonator with partial coverage of hydrogen sensitive material Pd/Pt layer.....  | 39 |
| Fig. 3.5 Results of the one-fourth covered ring resonator hydrogen sensor .....  | 40 |
| Fig. 3.6 Results of the half covered ring resonator hydrogen sensor.....   | 40 |
| Fig. 3.7 Results of the three-fourths covered ring resonator hydrogen sensor .....   | 41 |
| Fig. 3.8 The comparison of spectrum shape between different coverage proportions for the Pt-covered structure at 1% hydrogen concentration .....                           | 41 |
| Fig. 3.9 Results of the ring resonator hydrogen sensor with the width of sensitive material layer 100 nm .....   | 42 |
| Fig. 3.10 Electromagnetic field intensity distribution at resonance wavelength 1535 nm for Pt layer structure.....   | 43 |
| Fig. 4.1. Generic HCG structure .....  | 46 |
| Fig. 4.2. Results of structures with fill factor of 0.3 .....  | 48 |
| Fig. 5.1 Yee Lattice of FDTD method in electromagnetism.....   | 52 |

## ABSTRACT

This thesis introduces three main research projects completed by Dachuan Wu. All the study are based on numerical simulation method. This first two are based on integrated ring resonator, a novel, ultra-small size, and widely used component in the field of photonics, telecommunications, and sensing technology. Firstly, a nano-size particles position sensor is proposed. With two resonators placed on a chip, the rough position of dust particles can be obtained. An original designed parallel two rings structure and an improved cascaded double ring structure are both described. Secondly, a plasmonic hydrogen sensor is proposed, with the coating of a layer of hydrogen sensitive material, the ring resonator gain the ability to detect hydrogen. The coating proportion and layer width of coated layer are investigated. The third project is an attempt to design a wideband reflector with easy fabrication capability based on high contrast grating (HCG) subwavelength grating structure. However, the results show evidence of the impossibility of this design. All the results are based on Finite Difference Time Domain (FDTD) simulation method in electromagnetism. The detailed algorithm of FDTD method is also introduced. The entire thesis is structured as following: 1, introduction of ring resonator; 2, particle position sensor; 3, hydrogen sensor; 4, wideband reflector; 5, and introduction of FDTD method;

## Chapter I

### Introduction and Basic Theory of Integrated Ring Resonator

#### 1.1 Introduction

An integrated microring resonator is a set of small waveguides in which one waveguide is a closed loop coupled to the light input and light output. It is one of the most important photonic devices and has been widely investigated as optical switching and filters for telecommunications, biomolecule sensing and detection for biomedicine.

Different types of integrated micro resonators have been investigated and utilized by many research groups. The mostly used are micro ring resonator and micro disk resonator since they can be fabricated in CMOS compatible microelectronic process.

Micro ring resonators and Micro disk resonators have been discussed and studied since the early 1960s. Micro resonators were proposed in 1969 by Marcatili at Bell Labs. After that many groups have studied on micro ring resonators and it is still one of the most popular topics in photonics engineering.

#### 1.2 Basic Theory

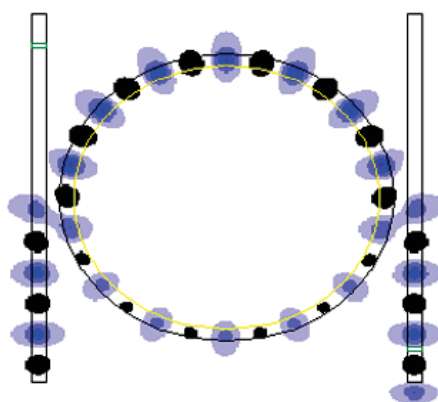


Fig. 1.1 Illustration of Integrated Ring Resonator



The propagation of electromagnetic wave (EM wave) is one of the most basic phenomena in nature. Its structure is as shown in Fig 1.2, the distribution of electrical field, magnetic field, and the direction of propagation are perpendicular to each other.

The behavior of EM wave can be described by Maxwell's equations:

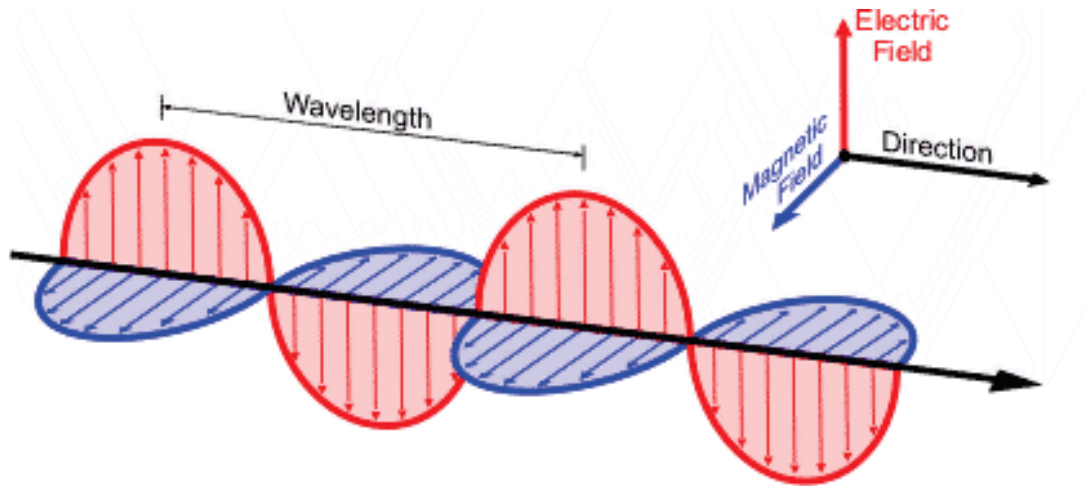


Fig. 1.2 Illustration of Electromagnetic Wave

$$\text{Gauss's Law: } \nabla \cdot \mathbf{E} = \frac{\rho}{\epsilon_0}, \quad (1.1)$$

$$\text{Gauss's Law for magnetism: } \nabla \cdot \mathbf{B} = 0, \quad (1.2)$$

$$\text{Maxwell–Faraday equation: } \nabla \times \mathbf{E} = -\frac{\partial \mathbf{B}}{\partial t}, \quad (1.3)$$

$$\text{Ampère's circuital law: } \nabla \times \mathbf{B} = \mu_0 \left( \mathbf{J} + \epsilon_0 \cdot \frac{\partial \mathbf{E}}{\partial t} \right), \quad (1.4)$$

where  $\epsilon_0$  is the permittivity of free space,  $\mu_0$  is the permeability of free space,  $\rho$  is electric charge density, and  $\mathbf{J}$  is the electric current density.

The propagation of EM wave is affected by the medium, which can be reflected by the two parameters permittivity  $\epsilon_0$  and permeability  $\mu_0$  in the equations above. Based on the distribution of medium in space, there is a structure which is widely applied in the communication industry, the waveguide. It is a structure that can limit the propagation of EM

wave. The simplest waveguide is planar waveguide. As shown in Fig 1.3, the refractive index of waveguide layer is much larger than it of environment medium, thus the EM wave which propagate in the waveguide layer would suffer total internal reflection when it go across the boundary of the medium. Hence, the EM wave is limited inside the waveguide layer.

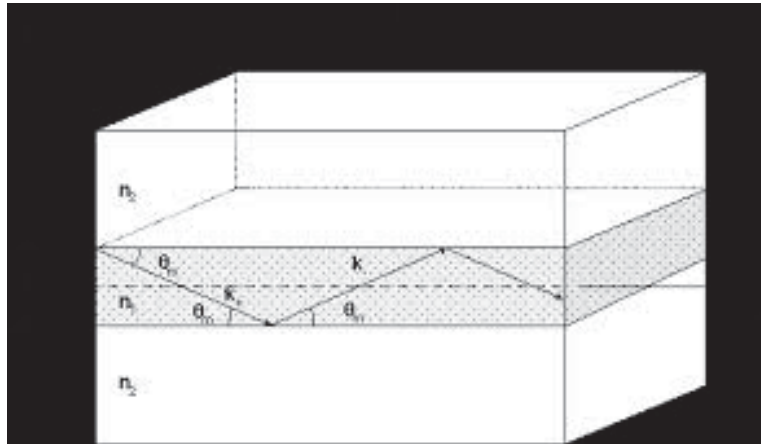


Fig. 1.3 Illustration of Planar Waveguide

The principle of the total internal reflection of light, or of the electromagnetic wave is well known. Here we utilize the concept of constructive interference to make a little deeper explanation. Fig 1.4 shows the explanation of the reflection and refraction of the light wave

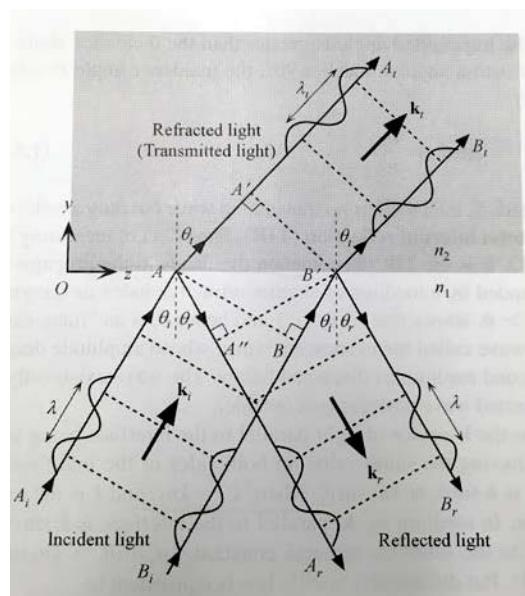


Fig. 1.4 Illustration of Reflection

by the concept of constructive interference. Here the input wave  $A_i$  and  $B_i$  have the same frequency and, they're in phase, their wavefront is shown as the dotted line in Fig 1.4. When these waves are reflected to become waves  $A_r$  and  $B_r$  then they must still be in phase, otherwise they will interfere destructively and destroy each other. The only way the two waves can stay in phase is if  $\theta_r = \theta_i$ . All other angles lead to the waves  $A_r$  and  $B_r$  being out of phase and interfering entirely or partially destructively.

The refracted waves  $A_t$  and  $B_t$  are propagating in a medium of refracted index  $n_2$  ( $< n_1$ ) that is different than  $n_1$ . Hence the waves  $A_t$  and  $B_t$  have different velocities than  $A_i$  and  $B_i$ . We consider what happens to a wavefront such as  $AB$ , corresponding perhaps to the maximum field, as it propagates from medium 1 to 2. We recall that the points  $A$  and  $B$  on this front are always in phase. During the time it takes for the phase  $B$  on wave  $B_i$  to reach  $B'$ , phase  $A$  on wave  $A_t$  has progressed to  $A'$ . The wavefront  $AB$  thus becomes the front  $A'B'$  in medium 2. Unless the two waves at  $A'$  and  $B'$  still have the same phase, there will be no transmitted wave.  $A'$  and  $B'$  points on the front are in phase only for one particular transmitted angle,  $\theta_t$ .

If it takes time  $t$  for the phase  $B$  on wave  $B_i$  to reach  $B'$ , then  $BB' = v_1 \cdot t = ct/n_1$ . During this time  $t$ , the phase  $A$  has progressed to  $A'$  where  $AA' = v_2 \cdot t = ct/n_2$ .  $A'$  and  $B'$  belong to the same front just like  $A$  and  $B$  so that  $AB$  is perpendicular to  $\mathbf{k}_i$  in medium 1 and  $A'B'$  is perpendicular to  $\mathbf{k}_t$  in medium 2. From geometrical considerations,  $AB' = BB'/\sin\theta_i$  and  $AB' = AA'/\sin\theta_t$  so that

$$AB' = \frac{v_1 \cdot t}{\sin \theta_i} = \frac{v_2 \cdot t}{\sin \theta_t}$$

or

$$\frac{\sin \theta_i}{\sin \theta_t} = \frac{v_1}{v_2} = \frac{n_2}{n_1}, \quad (1.5)$$

So here we come to the well-known **Snell's law**, which relates the angles of incidence and refraction to the refractive indices of the media.

When  $n_1 > n_2$  then obviously the transmitted angle is greater than the incidence angle

as apparent in Fig 1.4. When the refraction angle  $\theta_t$  reaches  $90^\circ$ , the incidence angle is called the **critical angle**  $\theta_c$ , which is given by

$$\sin\theta_c = \frac{n_2}{n_1}, \quad (1.6)$$

When the incidence angle  $\theta_i$  exceeds  $\theta_c$  then there is no transmitted wave but only a reflected wave. The latter phenomenon is called **total internal reflection (TIR)**. This is the explanation of TIR by the concept of constructive interference of wave.

Let's keep on the topic of the waveguide. Besides the most basic planar waveguide (it

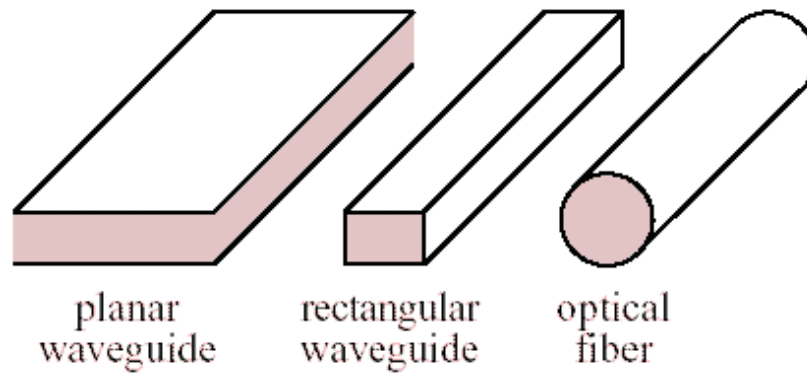


Fig. 1.5 Illustration of Waveguide

limits EM wave in only one dimension), by applying limitation on another dimension, we can obtain the rectangle waveguide, and the circular waveguide (the optical fiber). Thus the propagation of EM wave could be controlled like a line. Among them, the rectangle waveguide can perfectly fit the CMOS (Complementary metal–oxide–semiconductor) technology in semiconductor manufacturing industry, thus has the potential to conveniently integrated with other devices. This makes it valuable for research and application.

The chapter one in this thesis mainly introduce two design of sensors based on integrated ring resonator, and all the waveguides using in them are rectangle waveguides. The Finite Difference Time Domain (FDTD) method is selected to be the experimental method. In fact, all the results showing in this thesis are based on the FDTD simulation. As a result, the accuracy of the computational simulation is vital. The thesis will use an individual chapter (chapter five) to make an introduction of the FDTD method, and the explanation of the set of

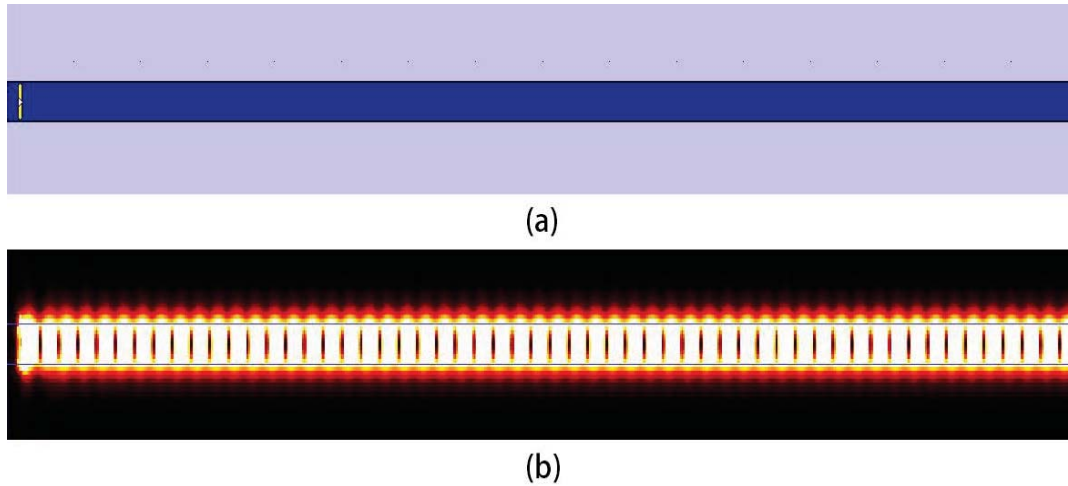


Fig. 1.6 Single Rectangle Waveguide. (a) Geometry structure; (b) Field distribution

parameters in simulations of the projects in this thesis.

As shown in Fig 1.6 (a), the most basic rectangle waveguide shows like a lone rectangle in the top view of a 2D FDTD simulation. Note that we set the coordinate system like this: positive x direction goes up, positive z direction goes right, and positive y direction goes towards us and be perpendicular to the paper, and a 2D simulation means we do not consider the variation of space in the y direction. We are going to use this coordinate system in all this thesis.

The light blue part in Fig 1.6 (a) expresses the air, with a refractive index of 1. Moreover, the dark blue part expresses silicon, with an approximate refractive index of 3.48 at the wavelength of 1550 nm, and with no absorption. The narrow yellow line at the left part of the waveguide is the EM wave excitor, the white arrow on it indicates its direction. In this figure, it excites a monochromatic continuous wave with wavelength at 1550 nm towards the right. Fig (b) illustrates the EM field intensity distribution in the waveguide after the whole device becomes a steady state. It can be seen that the simulation result agrees with the analysis by fluctuating optics, that the main part of EM wave is tracked inside the waveguide, besides that there exists the evanescent wave penetrates into the environment, which is air, with a certain length (which is pretty short).

Based on the theory of electromagnetism, several factors will affect the behavior of EM wave in a waveguide:

1. The property of the medium. It includes the relative permittivity  $\epsilon$ , absolute permittivity  $\epsilon_0$ , and the relative permeability  $\mu$ . For most of those general nonmagnetic materials, the relative permeability  $\mu$  would be 1, which means the absolute permeability of the material equals to the permeability in vacuum  $\mu_0$ . And the relative permittivity  $\epsilon$  could be expressed by the refractive index  $n$  and absorption coefficient  $a$ . Note that both the properties of waveguide medium and environment medium will affect the behavior.

2. The frequency of EM wave. The property of medium also varies with the variation of the frequency of EM wave. For a certain medium, we have to determine the frequency of applied EM wave before we determine its optical property.

3. The polarization of EM wave. For a rectangle waveguide, we can easily find the asymmetry along its tangential direction, because its cross section is a rectangle. In this condition, which directions that the electrical field and magnetic field distribute would make a large difference in the behavior of waveguide. Furthermore, all the simulations in this thesis are a 2D simulation, which means the influence of EM wave polarization would be much more serious. As a counter example, a waveguide which has a fully symmetric cross section, like a circular waveguide (optical fiber), is not affected by the polarization of EM wave.

4. The geometric structure of waveguide. In this thesis, all the waveguides are considered to be rectangle waveguide, and 2D simulation eliminates the influence of its depth,

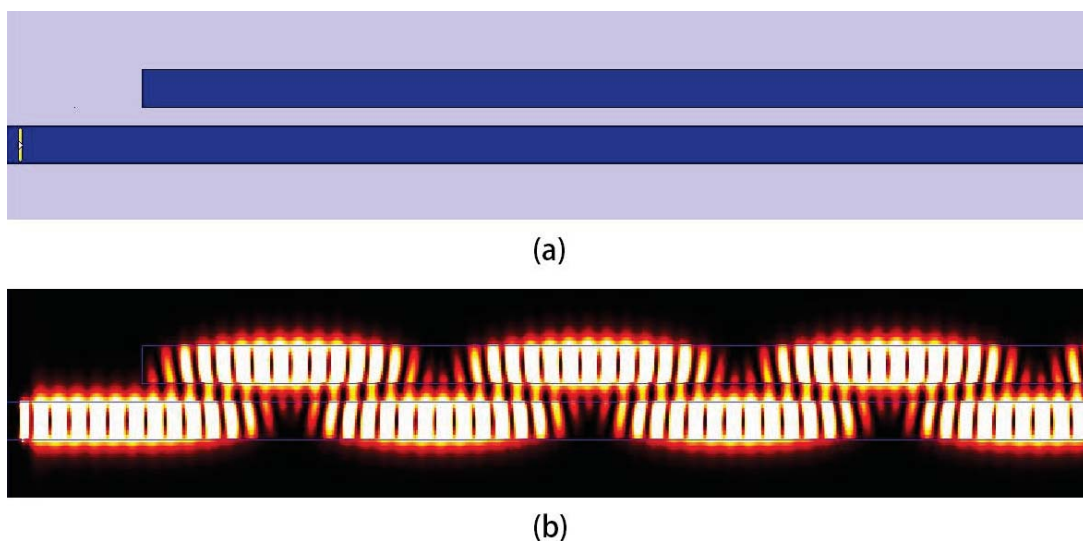


Fig. 1.7 Double Rectangle Waveguides. (a) Geometry structure; (b) Field distribution

the only geometric parameter of the waveguide that we need to consider is the width. This parameter mainly affected the propagation mode of EM wave inside the waveguide. Thus, in this thesis, we set all the waveguides to be 200 nm at width, ensuring they are single mode waveguides and there is no dispersion caused by different modes.

In the applications of the waveguide structure, the coupling of multi waveguides is widely researched and applied. As shown in Fig 1.7, when we place an extra long rectangle waveguide besides an original long rectangle waveguide, as long as the gap is sufficiently small, the phenomenon of coupling between waveguides would occur, that the EM energy which initially propagated in one waveguide will go across the gap of environment medium to the other waveguide, just like it go refracted to the other side. Then if the two waveguides keep going parallel, the EM energy will oscillate between the two waveguides, just like what Fig 1.7 (b) shows. Note the gap in this figure between the two waveguides is 100 nm.

This phenomenon can be roughly explained by the constructive interference of wave. As shown in Fig 1.8, the total internal reflection occurs whenever a wave is propagating in an optically denser medium, such as A in Fig 1.8, is incident at an angle greater than the critical angle at the interface AB with a medium B of lower refractive index. If we were to shrink the thickness  $d$  of medium B, we would observe that when B is sufficiently thin, an attenuated light beam emerges on the other side of B in C. This phenomenon in which an incident wave is partially transmitted through a medium where it is forbidden in terms of simple geometrical

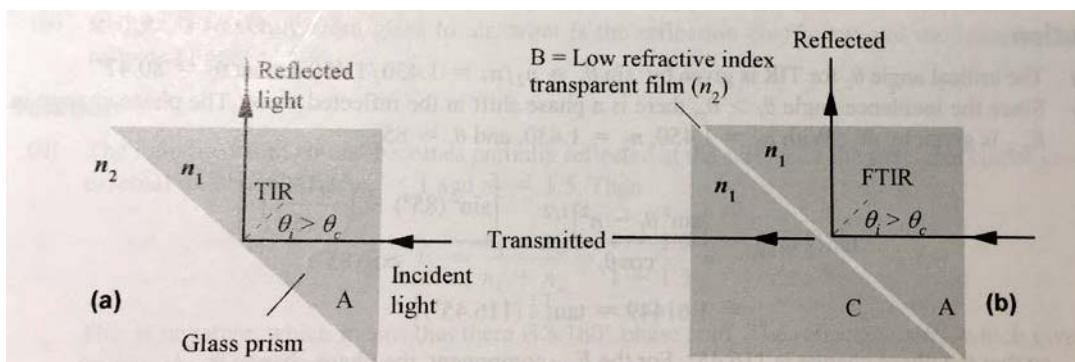


Fig. 1.8 Illustration of frustrated total internal reflection. (a) A light incident at the long face of a glass prism suffers TIR; the prism deflects the light. (b) Two prisms separated by a thin low refractive index film forming a beam-splitter cube. The incident beam is split into two beams by

optics is called **optical tunneling** and is a consequence of the electromagnetic wave nature of light. It is because the field of the evanescent wave penetrates into medium B and reaches the interface BC before it vanishes. The optical tunneling phenomenon is illustrated and is referred to as **frustrated total internal reflection (FTIR)**: the proximity of medium C frustrates TIR. The transmitted wave in C carries some of the light intensity, and thus the intensity of the reflected wave is reduced.

The further explanation of coupling phenomenon relies on detailed analysis of EM energy inside the waveguides, the concept of constructive interference is not enough for us to fully understand the coupling between waveguides. However, the theory of this concept is not the emphasis of this thesis, so the theoretical analysis of coupling would end up here.

The application of waveguide covers a wide range, among them, the sensing technology is an interesting area and has been widely researched. The basic mechanism can be simply explained in such way: by placing a waveguide into some environment medium, the medium would affect the evanescent wave of the waveguide and thus affect the EM wave inside the waveguide by changing its wavelength of intensity. Therefore, we could detect the variation of environment medium by detecting the variation of some parameter of EM wave in the

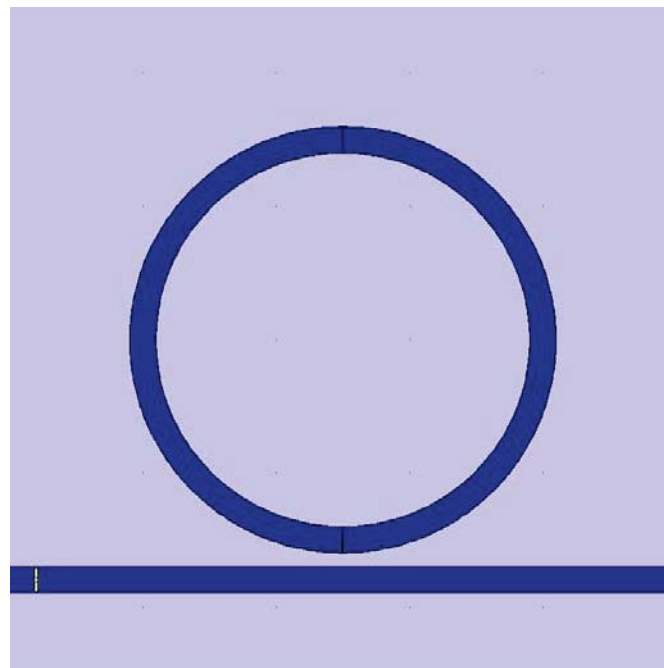


Fig. 1.9 Ring Resonator consists of a ring and a slab waveguide



waveguide. In this way, a sensor based on waveguide could be designed as long as we can figure out the relationship between the variation of what we want to detect, for example, the concentration of  $\text{CO}_2$  in air, and the variation of EM wave, for example, its intensity.

However, the speed of EM wave in the waveguide is so fast, that the variation of medium would result in a very small change of the EM wave. The application of ring resonator gives a solution of this problem to some extent. As shown in Fig 1.9, by adding a ring waveguide besides a long rectangle waveguide (which we call the slab waveguide), the basic model of ring resonator is obtained. Note that the ring waveguide is still a rectangle waveguide because of the shape of its cross section. The property of ring resonator can also be roughly explained by the concept of constructive interference. Because the ring waveguide is a kind of closed waveguide, the EM wave propagated in it have to fit constructive interference in the whole ring. This turns to an equation which the wavelength of EM wave inside the ring should fit:

$$n_{\text{eff}} \cdot L = m \cdot \lambda, \quad (1.7)$$

where  $n_{\text{eff}}$  is the effective refractive index of ring waveguide,  $L$  is the length of the light path inside the ring, which approximately equals to the circumference of the ring,  $m$  is

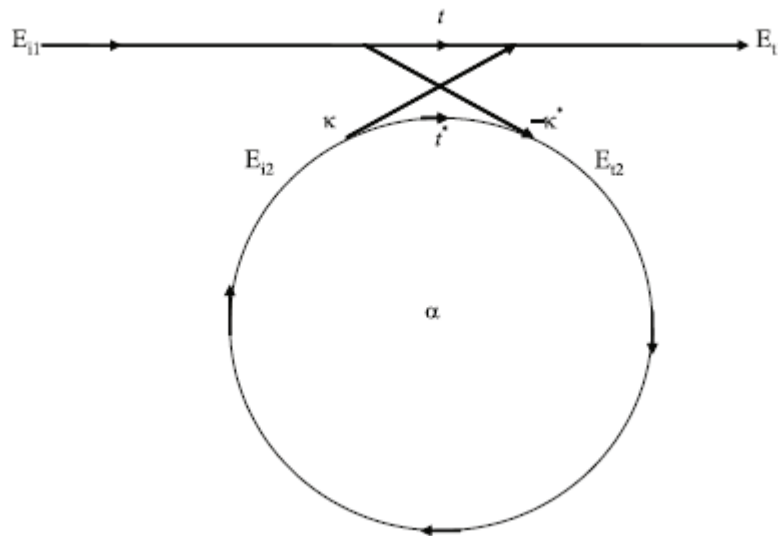


Fig. 1.10 Model of a single ring resonator with one waveguide

an integer, and  $\lambda$  is the wavelength in vacuum of the EM wave. The wavelengths described by this equation is what we call the resonance wavelength or coupling wavelength.

Based on the equation (1.7), only certain wavelengths of EM wave could fit the coupling condition of the ring resonator. These wavelengths become the peak wavelength in the output spectrum of the ring resonator. Also, by increasing the gap between ring and slab waveguide, the Q-factor of the peaks could be improved.

According to electromagnetism, we can make a further analysis of ring resonator.

Fig 1.10 shows the basic configuration of the ring resonator, which consists of unidirectional coupling between a ring resonator with radius  $r$  and a waveguide. Defining that a single unidirectional mode of the resonator is excited, the coupling is lossless, single polarization is considered, none of the waveguide segments and coupler elements couple waves of different polarization, the various kinds of losses occurring along the propagation of light in the ring resonator filter are incorporated in the attenuation constant, the interaction can be described by the matrix relation:

$$\begin{pmatrix} E_{t1} \\ E_{t2} \end{pmatrix} = \begin{pmatrix} t & k \\ -k^* & t^* \end{pmatrix} \begin{pmatrix} E_{i1} \\ E_{i2} \end{pmatrix}, \quad (1.8)$$

The complex mode amplitudes  $E$  are normalized so that their squared magnitude corresponds to the modal power. The coupler parameters  $t$  and  $k$  depend on the specific coupling mechanism used. The  $*$  denotes the conjugated complex value of  $t$  and  $k$ , respectively.

The matrix is symmetric because the networks under consideration are reciprocal. Therefore

$$|k^2| + |t^2| = 1, \quad (1.9)$$

To further simplify the model,  $E_{i1}$  is chosen to be equal to 1. Then the round trip in the ring is given by

$$E_{i2} = a \cdot e^{j\theta} \cdot E_{t2}, \quad (1.10)$$

where  $a$  is the loss coefficient of the ring (zero loss:  $a=1$ ) and  $e^{j\theta}$  represents the phase change in one round trip, note that this  $a$  is not the absorption coefficient in material science.

Thus, the  $E_{i2}$ ,  $E_{t1}$ , and  $E_{t2}$  can be solved

$$E_{i1} = 1, \quad (1.11)$$

$$E_{t1} = \frac{-a+t \cdot e^{-j\theta}}{-a \cdot t + e^{-j\theta}}, \quad (1.12)$$

$$E_{i2} = \frac{-a \cdot k^*}{-a \cdot t^* + e^{-j\theta}}, \quad (1.13)$$

$$E_{t2} = \frac{-k^*}{1 - a \cdot t^* \cdot e^{-j\theta}}, \quad (1.14)$$

These lead to the transmission power  $P = |E|^2$  in the waveguides, which are:

$$P_{i1} = 1, \quad (1.15)$$

$$P_{t1} = \frac{a^2 + |t|^2 - 2a|t| \cdot \cos(\theta + \varphi_t)}{1 + a^2|t|^2 - 2a|t| \cdot \cos(\theta + \varphi_t)}, \quad (1.16)$$

$$P_{i2} = \frac{a^2 \cdot (1 - |t|^2)}{1 + a^2|t|^2 - 2a|t| \cdot \cos(\theta + \varphi_t)}, \quad (1.17)$$

$$P_{t2} = \frac{1 - |t|^2}{1 + a^2|t|^2 - 2a|t| \cdot \cos(\theta + \varphi_t)}, \quad (1.18)$$

A normal assumption in the ideal condition is that the material of waveguide has no absorption of EM wave, which means  $a = 1$ . It could be noticed that in this condition, equation 1.16 becomes  $P_{t1} = 1$ , thus the input EM energy in the slab waveguide equals to the output EM energy at always. The participation of ring waveguide in this device makes no effect on the output. However, in real application, the absorption of EM wave always exists due to both the environmental factor and the material itself, although it's extremely small. In resonator, EM energy could be tracked inside the ring for a long time, thus the negligible absorption of EM energy is amplified, and the existing of ring waveguide does make an effect on the output.

For those EM waves whose wavelength fit the coupling condition,  $(\theta + \varphi_t) = 2\pi m$ ,

where  $m$  is an integer, the following is obtained

$$P_{t1} = \frac{(a-|t|)^2}{(1-a|t|)^2}, \quad (1.19)$$

$$P_{i2} = \frac{a^2 \cdot (1-|t|^2)}{(1-a|t|)^2}, \quad (1.20)$$

A special case happens when  $a = |t|$  in (1.17), when the internal losses are equal to the coupling losses. The transmitted power  $P_{t1}$  becomes 0. This is known in literature as critical coupling, which is due to destructive interference.

The experiment part of this thesis is totally done by computation simulation. So normal materials could be approximately assumed to be in ideal condition, which means no absorption and isotropic. In this case, the basic ring resonator with only one slab waveguide and one ring waveguide is not valuable. Therefore, a structure which is more suitable for simulation is required. By adding an extra slab waveguide at the other side of ring waveguide, we get another basic model of the ring resonator, which is shown in fig 1.11. Moreover, this model is the most widely used model in real application and research.

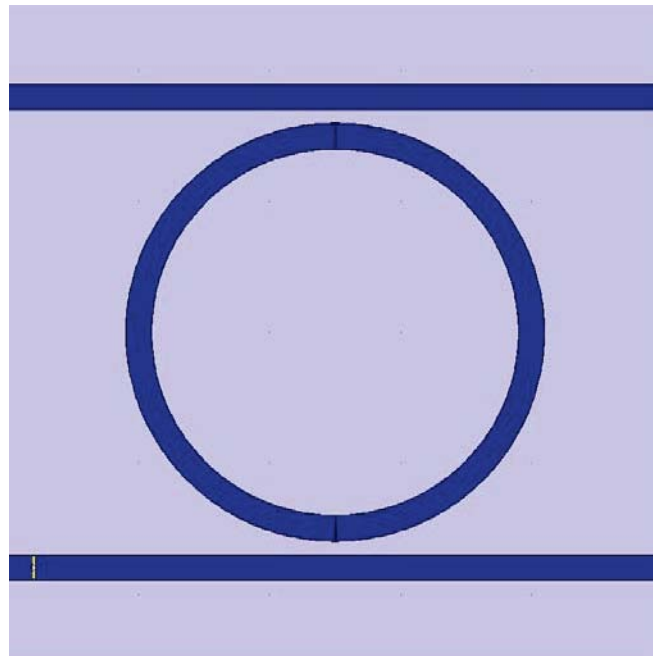


Fig. 1.11 Ring Resonator consists of a ring and two slab waveguide

This model is pretty similar to the previous model. The coupling condition between the input waveguide and ring waveguide is still following equation (1.7). The difference is that the extra slab waveguide gives an exit to EM energy in the ring waveguide. By utilizing the same analysis method, we can get following results.

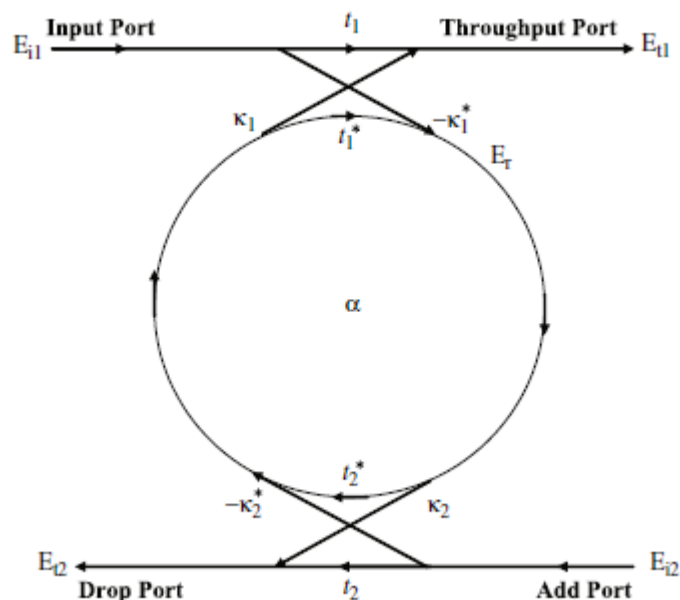


Fig. 1.12 Model of a basic add-drop single ring resonator filter

As shown in fig 1.12, the coupling coefficient between input waveguide and ring, output waveguide and ring both follow equation (1.8) and (1.9), the subscripts denote the difference. Note that for ideal condition, the  $t_1$  and  $k_1$ ,  $t_2$  and  $k_2$  in fig 1.11 are equal to each other respectively.

Let  $E_{i1} = 1$ ,  $E_{i2} = 0$ , and  $a = a_{1/2}^2$ ,  $\theta = 2 \cdot \theta_{1/2}$ , the following could be obtained:

$$E_{i1} = 1, \tag{1.21}$$

$$E_{t1} = \frac{-a \cdot t_2^* + t_1 \cdot e^{-j\theta}}{-a \cdot t_1^* \cdot t_2^* + e^{-j\theta}}, \tag{1.22}$$

$$E_{i2} = 0, \tag{1.23}$$

$$E_{t2} = \frac{-a_{1/2} k_1^* \cdot k_2 \cdot e^{-j\theta_{1/2}}}{-a \cdot t_1^* \cdot t_2^* + e^{-j\theta}}, \tag{1.24}$$

and the energy equations for each ports:

$$P_{i1} = 1, \quad (1.25)$$

$$P_{t1} = \frac{|t_1|^2 + a^2 \cdot |t_2|^2 - a|t_1| \cdot |t_2| \cdot \cos(\theta + \varphi_{t1})}{1 + a^2|t_1|^2 \cdot |t_2|^2 - a|t_1| \cdot |t_2| \cdot \cos(\theta + \varphi_{t1})}, \quad (1.26)$$

$$P_{i2} = 0, \quad (1.27)$$

$$P_{t2} = \frac{a \cdot (1 - |t_1|^2) \cdot (1 - |t_2|^2) \cdot \cos(\theta + \varphi_{t2})}{1 + a^2|t_1|^2 \cdot |t_2|^2 - a|t_1| \cdot |t_2| \cdot \cos(\theta + \varphi_{t2})}, \quad (1.28)$$

It could be found that even in the ideal condition where  $a = 1$ , the phenomenon that  $P_{t1}$  always equals to 1 will not happen. When the wavelength of EM wave fits the coupling condition, we have  $(\theta + \varphi_{t1}) = 2\pi m$ , and  $(\theta + \varphi_{t2}) = 2\pi m$ , where  $m$  is an integer, the following is obtained

$$P_{t1} = \frac{(|t_1| - a|t_2|)^2}{(1 - a|t_1 \cdot t_2|)^2}, \quad (1.29)$$

$$P_{t2} = \frac{a^2 \cdot (1 - |t_1|^2) \cdot (1 - |t_2|^2)}{(1 - a|t_1 \cdot t_2|)^2}, \quad (1.30)$$

The throughput port mode amplitude  $E_{t1}$  (1.20) will be zero at resonance for identical symmetrical couplers  $t_1 = t_2$  if  $a = 1$ , which indicates that the wavelength on resonance is fully extracted by the resonator. In real condition, the value of  $a = 1$  can only be achieved by the implementation of gain incorporated in the ring resonator to compensate the waveguide losses. (However, in ideal condition, for example, in simulation,  $a$  can always be 1.) The value of the loss coefficient  $a$  is fixed in a purely passive ring resonator. A possibility of achieving minimum intensity ( $P_{t1} = 0$ ) at resonance of the output transmission  $P_{t1}$  at the throughput port is to adjust the coupling parameters  $t_1$ ,  $t_2$  to the loss coefficient  $a$ . From (1.20) we obtain

$$a = \left| \frac{t_1}{t_2} \right|, \quad (1.31)$$

If the ring resonator is lossless ( $a = 1$ ), then the couplers have to be symmetric in order to achieve minimum intensity. The transmission spectrum of a lossless ring resonator with

radius of  $r = 1.5 \mu\text{m}$  and coupling gap of 100 nm is shown in Fig 1.14

Ring resonators can be described by certain figures of merit which are also generally used to describe optical filters. For simplicity, this thesis just gives the general definition and equation of these figures.

First, the distance between resonance peaks, which is called the free spectral range (FSR), it can be solved by:

$$FSR = \Delta\lambda \approx \frac{\lambda^2}{n_{\text{eff}} \cdot L}, \quad (1.32)$$

Second, the resonance width which is defined as the full width at half maximum (FWHM) or 3 dB bandwidth  $2\delta\lambda$  of the resonance lineshape.

$$FWHM = 2\delta\lambda = \frac{k^2\lambda^2}{\pi L n_{\text{eff}}}, \quad (1.33)$$

Another parameter which can now be directly calculated from the parameters in the previous chapter is the finesse  $F$  of the ring resonator filter. It is defined as the ratio of the FSR and the width of a resonance for a specific wavelength (FWHM):

$$F = \frac{FSR}{FWHM} = \frac{\Delta\lambda}{2\delta\lambda} \approx \frac{\pi}{k^2}, \quad (1.34)$$

A parameter which is closely related to the finesse is the quality factor  $Q$  of a resonator, which is a measure of the sharpness of the resonance. It is defined as the ratio of the

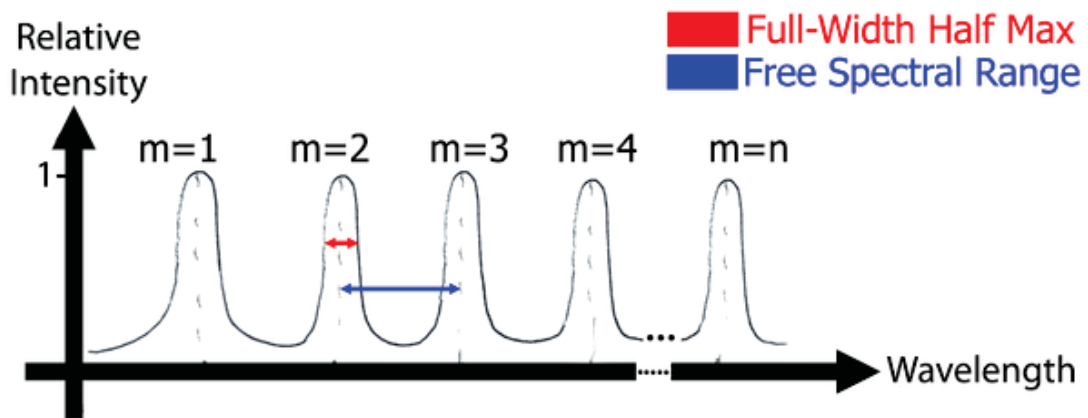


Fig. 1.13 Illustration of Full-Width at Half Maximum and Free Spectral Range.

operation wavelength and the resonance width

$$Q = \frac{\lambda}{2\delta\lambda} = \frac{n_{eff} \cdot L}{\lambda} \cdot F, \quad (1.35)$$

Above is the basic theory of integrated ring resonator. There exist several variants of the ring resonator, such as disk resonator and racetrack resonator. As the name implies, they are just simply using disk waveguide or racetrack shape waveguide to replace the ring waveguide. The analysis method of them is similar to the method we used, and their output spectrum is also similar to that of the standard ring resonator. So we are not going to make analysis for them. Fig 1.14 shows the simulation result of the structure in fig 1.11. Fig 1.14 (a) shows the spectrum of throughput port, which is denoted as T1 in fig 1.12, and fig 1.14 (b) shows the drop port spectrum, which is denoted as T2. It can be observed that the peaks in the T1 spectrum are downwards, and in T2 are upwards. The result agrees with the description by equation (1.7) that the wavelengths which fit the coupling condition propagate through the ring waveguide to the output waveguide, and the rest stay in the original input waveguide. In this case, the refractive index of the waveguide is chosen to be 3.48, the width of waveguides is 200 nm, the radius of ring waveguide is 1500 nm, and the gap between waveguides is 100.

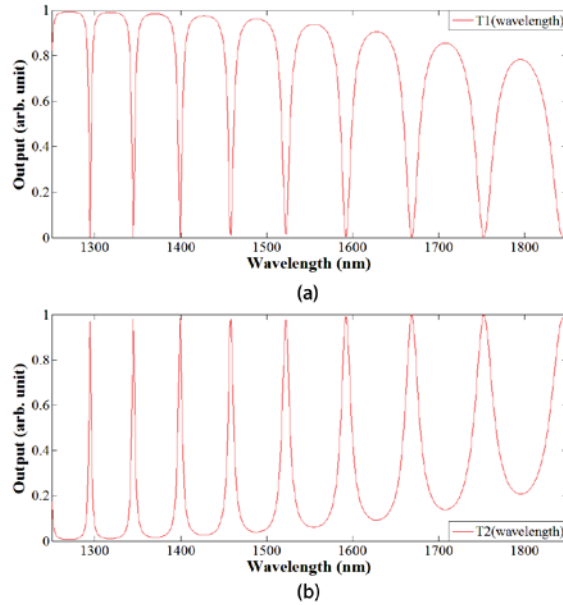


Fig. 1.14 Transmission spectrum of the ring resonator. (a) T1 port, (b) T2 port.



## Chapter II

### Particle position sensor based on integrated double ring resonator

This chapter introduces a design of particle position sensor. In traditional method, an SEM detection is needed to detect particles in tens of nanometers. This design proposes an easier method to detect the rough position of particles by utilizing the double resonators structure with no need of SEM. In this chapter, both a basic parallel double resonators structure and an improved cascaded double resonators structure are proposed.

#### 2.1 Basic design

The configuration of the sensor is shown in Fig 2.1. Based on the traditional single ring

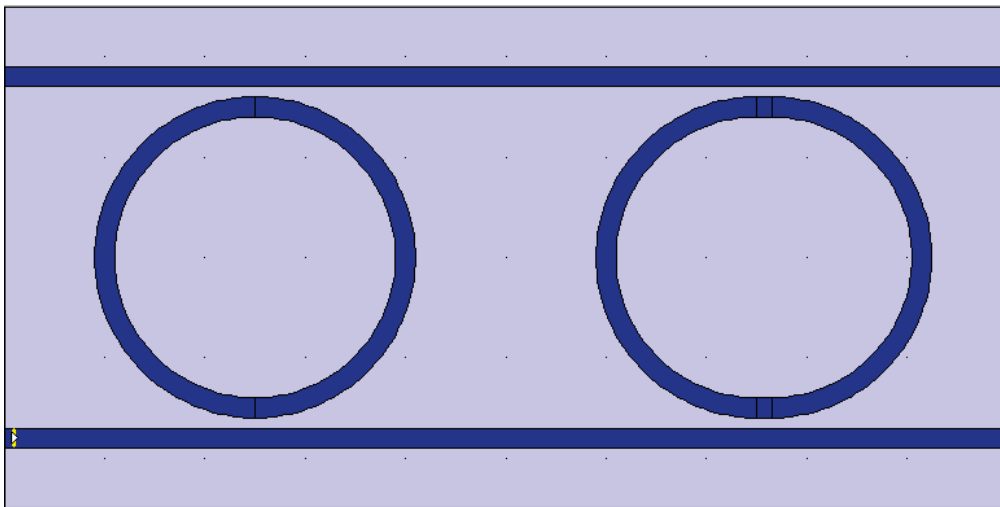


Fig. 2.1. Particle position sensor based on parallel double ring resonator

resonator, another racetrack resonator waveguide is added between the two slab waveguides. According to equation (1.7), to have some difference in the output of the two resonators in the same material, we have to made their circumferences a little different. Therefore, this design utilizes a racetrack as the second resonator. The racetrack resonator is consist of two semicircular waveguides and

two short straight waveguides. The two semicircular waveguides are in exactly same shape with the ring resonator, with a radius of 1500 nm, and the two straight waveguides are set to be 150 nm in length, to let the wave peaks in output spectrum which is generated by the two resonators distributed most separately. The effective refractive index of the waveguides is set to be 3.00, which is contributed by the Si waveguides on SiO<sub>2</sub> substrate. As said before, the width of all the waveguides is 200 nm, to ensure the EM wave propagated in the waveguides is single mode. The gap between resonators and slab waveguides is 200 nm, and the distance between two resonators is 5000 nm measured from the same side of the resonators so that there's no direct coupling between two resonators.

Let's recall the analysis of ring resonator in previous chapter, the light source at input waveguide is denoted as  $I_1$  or simply as  $I$ , the output on the other end of input waveguide is denoted as  $T_1$ , and the output at output waveguide is denoted as  $T_2$ . As shown in Fig 2.1, we use subscript l and r to denote the ring resonator on left and the racetrack resonator on the right.

Input EM wave enters the device from the left end of the input waveguide at the bottom

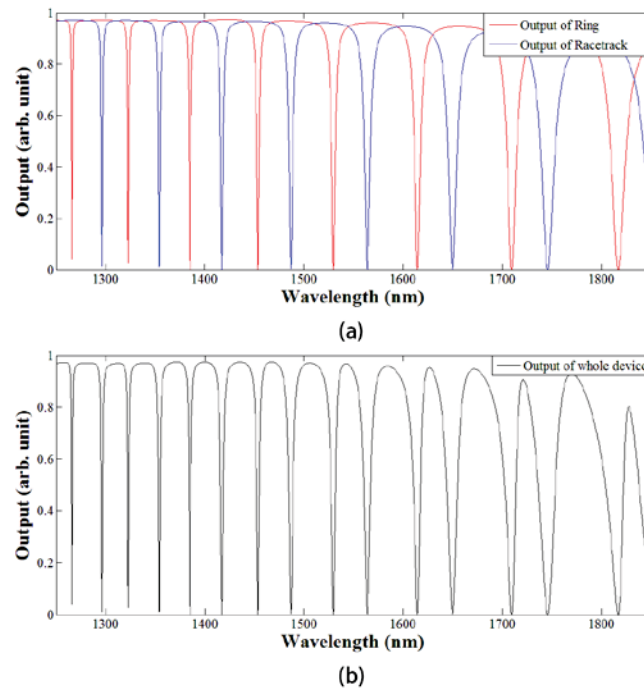


Fig. 2.2. Output of the device. (a) Output of the two resonators, respectively. (b) Output of the whole device.

of Fig 2.1. When the wave goes by the ring resonator, the part of the wave whose wavelength can fit the coupling condition propagates into the ring waveguide, and the rest keep propagation in the input waveguide towards to the right. Moreover, then, after going by the racetrack resonator, the output at input waveguide approximately follows the equation

$$T_{\text{total1}} \approx T_{\text{l1}} \cdot T_{\text{r1}}, \quad (2.1)$$

Fig 2.2 shows the output spectrum of this device, which is measured at the right end of the input waveguide. In (a) the red line expresses the spectrum formed by the ring resonator itself, and the blue line expressed the spectrum formed by the racetrack resonator itself. Fig (b) shows the spectrum formed by the whole device, it can be found that every peak in Fig (b) corresponds to a peak in Fig (a), and the peaks coming from the ring (red line) and those coming from racetrack (blue line) exist alternatively.

In theory, there exists a part of EM wave whose wavelength does not fit critical coupling condition of either the two resonators doesn't couple into the ring resonator when passes by it firstly, and keeps propagating along input waveguide, when it arrives the racetrack resonator, it couples into the racetrack, and comes to the output waveguide propagating towards left, then couples into ring resonator when it passes by the ring secondly. Theoretically, this part of EM wave can exist in the device forever as long as there's no absorption in the device. However, due to the fact that this part of EM wave does not fit critical coupling of either the

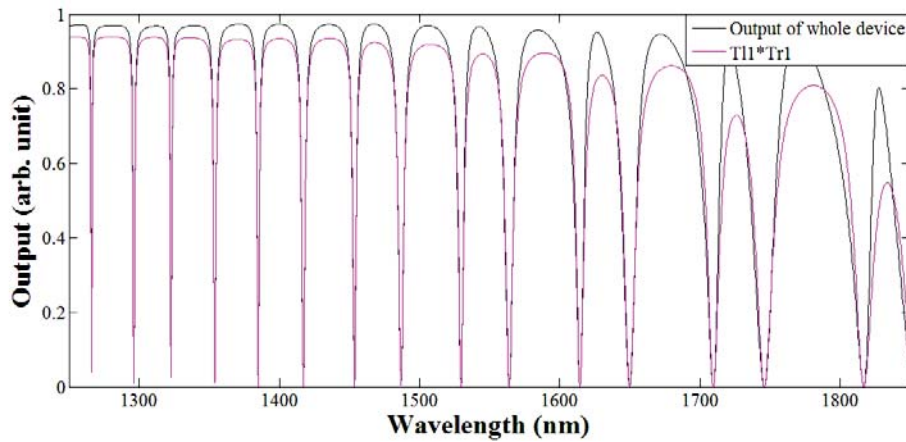


Fig. 2.3. Comparison between the real output and  $T_{l1} \cdot T_{r1}$ .

two resonator, it attenuates a little every time it couples. Thus we can determine that this part of EM wave is so weak that can be neglected. So we do not need to worry about this part of EM wave, especially when our focus is on the peaks in the output spectrum. Fig 2.3 shows the difference between the real output and theoretical value of  $T_{11} \cdot T_{r1}$ , the black line is the real output. It can be found that the difference is mainly at the wave troughs, and there's almost no difference at peaks.

According to the discussion above, the whole output approximately equals to the product of the outputs of two resonators themselves, especially at each wave peaks. Moreover, because the two resonators are designed to generate most separately peaks, so in the whole output, the peaks are generated when the output of one resonator is 0 while the output of the other is close to 1. Thus we can infer that if the output of one resonator shifts for a little wavelength while the other doesn't, it will be reflected in the whole output as those peaks coming from this resonator shifts, but the other peaks does not.

This phenomenon offers this device the capability to detect the position of particles.

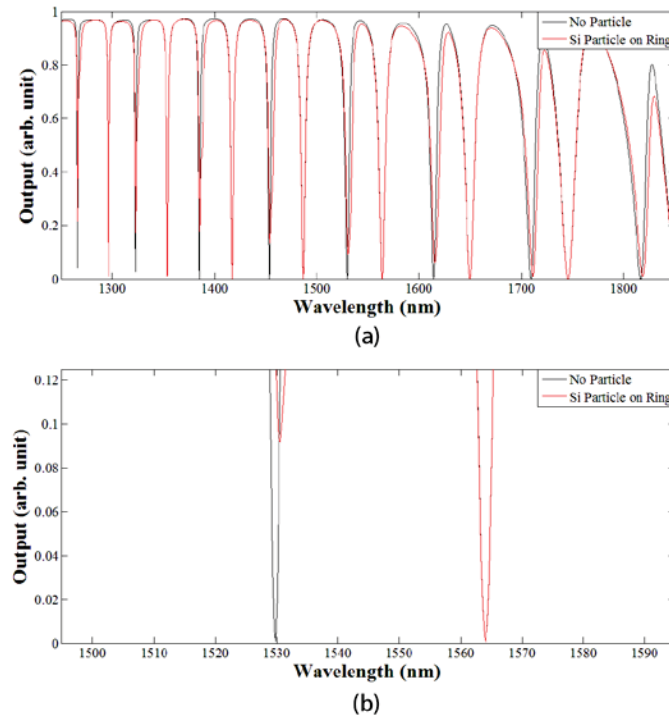


Fig. 2.4. Output of the device when a Si particle exists close to ring resonator. (a) Whole output at wavelength from 1250 nm to 1850 nm. (b) The two peaks around 1550 nm.

When there're some particles appear close to one resonator, because they will affect the evanescent wave of the resonator, the effective refractive index of this resonator is changed. Moreover, according to equation (1.7), the output spectrum of this resonator will shift a little. Thus, by observing the output spectrum of the whole device, we can determine which resonator the particles is close to. Also, due to the sensitivity of ring resonator to the environment, particles in nano size can be detected. In this basic design, the two resonators are like two pixels on the whole device (for example, a chip), and we can find out which pixel the particles located on. In theory, we can add more resonators to add the pixels as long as the peaks generated by the resonators can be distinguished clearly. However, the design of this particle position sensor needs the assumption that the particles will not affect both the two resonators simultaneously.

Let's make an example with a dielectric particle. In simulation we add a circular Si particle with a diameter of 100 nm close to ring resonator, it shows in the 2-dimensional image as a circle. The optical parameters are set to be  $n = 3.477, a = 0/cm$ . Fig 2.4 shows

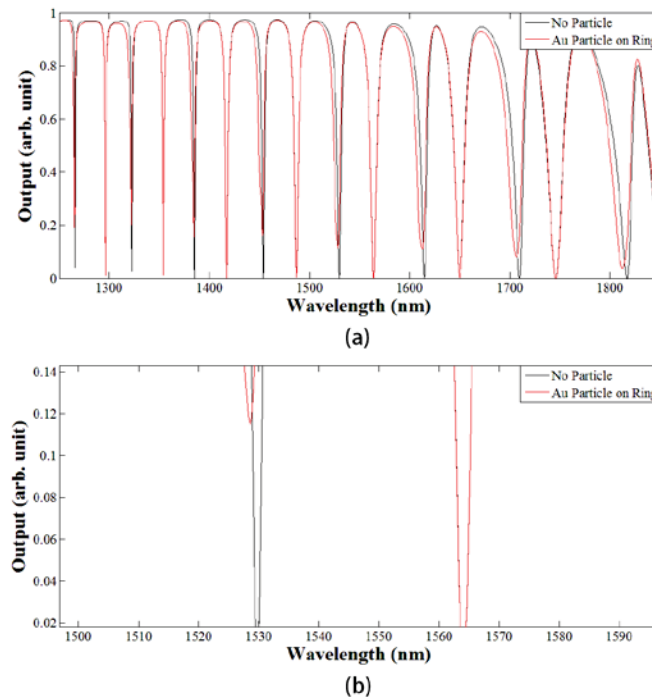


Fig. 2.5. Output of the device when an Au particle exists close to ring resonator. (a) Whole output at wavelength from 1250 nm to 1850 nm. (b) The two peaks around 1550 nm.

the output spectrum of this simulation, the black line in figure is the original spectrum when no particles exist, and the red line is the spectrum after adding the particle. We can find in Fig (a) that the peaks generated by ring resonator all occur a corresponding shift, while the other peaks have no difference. Fig (b) is the enlarged figure to show the adjacent peaks at 1529.81 nm and 1664.08 nm. According to Fig 2.2, the peak on left is generated by ring resonator, and the peak on right is generated by racetrack resonator. It is clear that after the adding of particle, the peak from ring resonator has a obvious shift, while the peak from racetrack almost overlaps the original spectrum. In this condition, the peak at 1529.81 nm has a red shift of approximate 0.77 nm to 1530.58 nm.

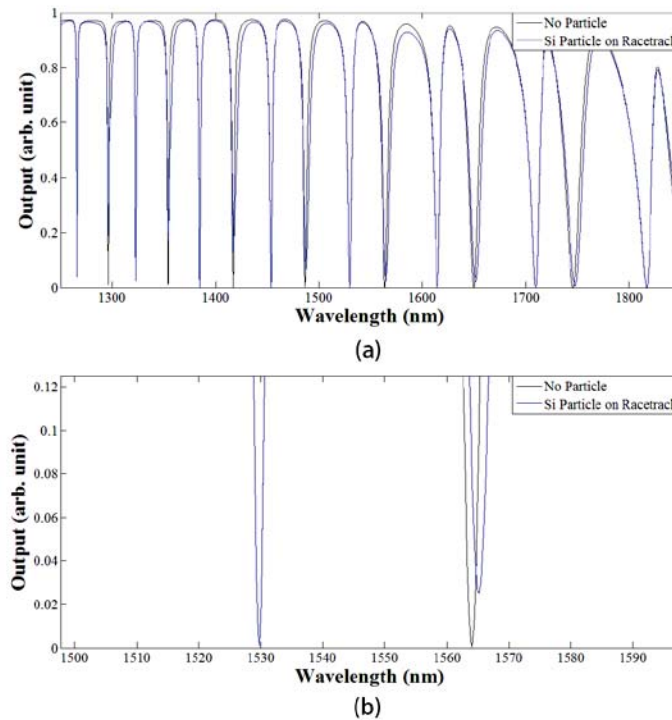


Fig. 2.6. Output of the device when a Si particle exists close to racetrack resonator. (a) Whole output at wavelength from 1250 nm to 1850 nm. (b) The two peaks around 1550 nm.

The existing of Si particle increases the effective refractive index of the ring resonator, and thus results in a red shift of its output. On the other hand, if there's a metallic particle (which has a refractive index lower than 1) exists close to the ring, the effective refractive index will be reduced, and the output spectrum will have a blue shift. Fig 2.5 shows this

result, in this simulation, an Au particle with the same size and same position replaces the previous Si particle, and the optical parameters are set to be  $n = 0.524$ ,  $a = 870930/cm$ . Due to the reduction of effective refractive index, the output of ring resonator occurs a blue shift. In the whole output, the peak at 1529.81 nm blue shift approximate 1.28 nm to 1528.53 nm.

Fig 2.6 and 2.7 shows the simulation results when placing the same Si and Au particle close to racetrack resonator. It could be found that the results are similar to previous results. For racetrack resonator, when a particle exists close to it, the effective refractive index of it is changed, and thus its output spectrum shifts. While in the whole output, the peaks generated by racetrack have a corresponding shift, and the other peaks stay in place. When a Si particle is existing, the peak at 1564.08 nm has a red shift of 1.08 nm to 1565.16 nm, while the peak at 1529.81 nm does not move. Moreover, when an Au particle is existing, the peak at 1564.08 nm blue shift 1.06 nm to 1563.02 nm.

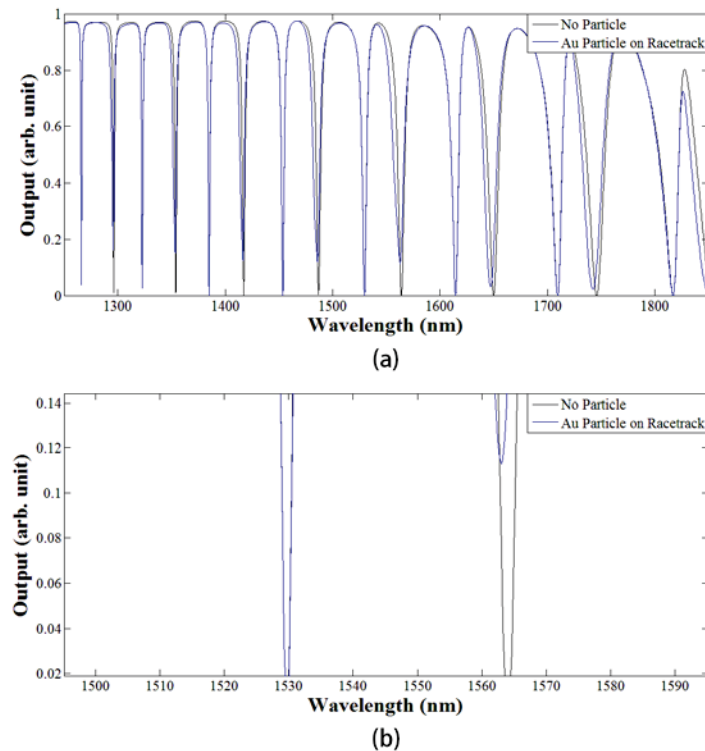


Fig. 2.7. Output of the device when a Au particle exists close to racetrack resonator. (a) Whole output at wavelength from 1250 nm to 1850 nm. (b) The two peaks around 1550 nm.

As discussed above, as long as we have the assumption that only one resonator is affected, we can gain the information of which resonator it is by observing the output spectrum. By tracking the wavelength shift of each peak, both the information of which resonator is affected and what type of this effect, which refers to particle types of metallic and dielectric, can be detected.

When a particle exists close to a resonator, the medium of that place is replaced by the particle material. Thus the effective refractive index of the whole resonator is changed. So we can infer, when the number of particles increases, the variation of effective index  $\Delta n_{eff}$  is positive proportional to this quantity, as long as the type (metallic or dielectric) and size of particles are same. Therefore, if we have the assumptions that only one type of particles will exist, and they will affect only one resonator, this design is able to be functionalized.

One thing worth to mention is that this design also has the function of self-referencing. There's a common problem on traditional spectrum based sensor that sometimes it is hard to distinguish whether a shift is caused by what we want to detect or the environment interference. In another word, the environment may interfere the function of these kinds of sensors. However, this design can effectively avoid this problem. As described above, the existence of particles will affect only one resonator, which results in only part of the peaks in spectrum shift. However, the interference from the environment will affect on two resonators simultaneously and results in a shift of all the peaks in the spectrum. Thus, when this device is being used, and some of the peaks do have a shift, by observing whether all the peaks in the out spectrum shift, we can infer whether the shift is causing by environment interference or not. Therefore, this design can eliminate the environment interference by itself, which we normally call self-reference.

From Fig 2.2 we can see, the peaks generated by the two resonators distributed separately, so as long as the applied light source has a wavelength bandwidth which is wide enough to cover arbitrary two peaks, the device can work.

## **2.2 Design based on Cascaded Ring Resonators**



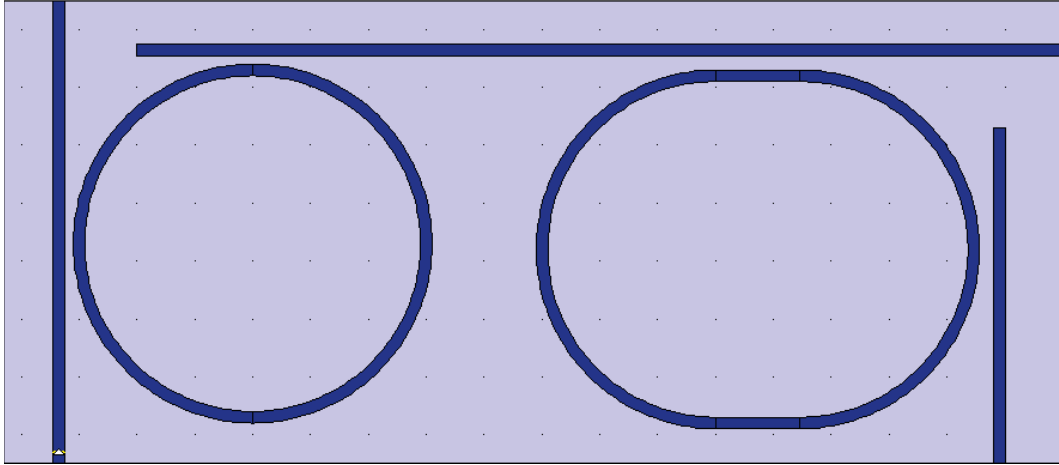


Fig. 2.8. Particle position sensor based on cascaded double ring resonator

In above simulations, the particles used are all spherical particles with a diameter of 100 nm. However, in a real application, there may exist smaller particles, of the refractive index of particles may have a smaller difference to air than Si or Au, in these conditions, the peak shift in output spectrum will be smaller. In the other word, we might need a high-resolution spectrometer on the detection end, which will significantly raise the cost of the device.

In this condition, an improvement of the design is proposed. As shown in Fig 2.8, the relative position of the two resonators remains, but the radius of the arcs is increased to twice, which is 3000 nm, to ensure the peaks generated by the two resonators more intensive. The slab waveguides are changed. In this new design, the input EM wave enters the device from the left bottom corner, propagates upwards and then comes to the top slab waveguide by the coupling of the ring resonator, and finally reaches the output end at the right bottom corner by the coupling of racetrack resonator.

As the main difference between this design and the previous one, the input of racetrack resonator becomes the  $T_2$  the output of ring resonator instead of  $T_1$  of the ring resonator. In this design, the measured signal is detected from the right bottom corner illustrated in Fig 2.8, and it satisfies the following equation:

$$T_{\text{total}} = T_{l2} \cdot T_{r2}, \quad (2.2)$$

In this design, there's no EM wave which could propagate circularly inside the device, so we use the equal sign in equation (2.2). The width of each waveguide is still 200 nm, to ensure they work in single mode. The gap between ring and slab waveguides is 150 nm, and the gap between racetrack and slab waveguides is 250 nm, with this configuration the two resonators will generate peaks with similar q-factor, which means similar shape. The length of the straight waveguide of racetrack resonator is set to be 1460 nm so that the two resonators have a different circumference and both generate a peak at 1660 nm.

The main purpose of this design is to reduce the requirement of the resolution of

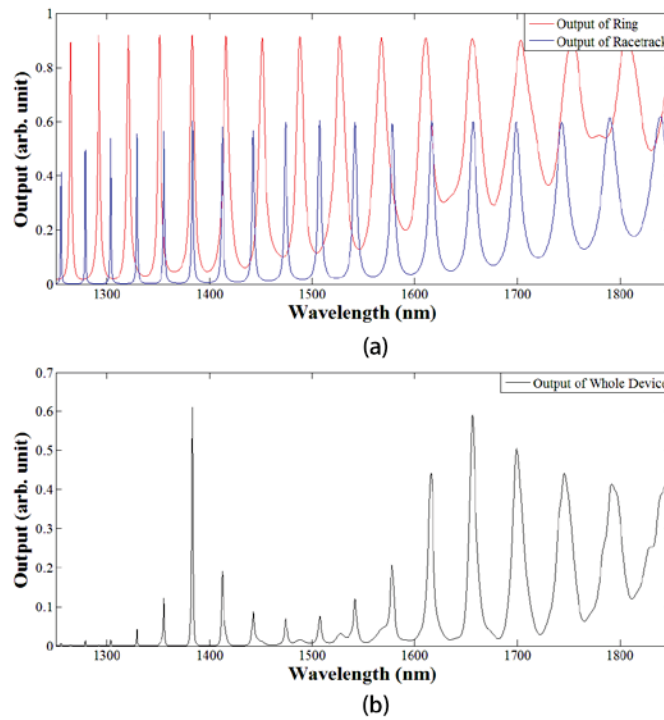


Fig. 2.9. Output of the device. (a) Output of the two resonators, respectively. (b) Output of the whole device.

spectrometer we use and thus reduce the cost of this device, so in this part, when we need to introduce the wavelength of some peaks, the accuracy will be in 5 nanometers, as an equivalent to the low-resolution spectrometer. Fig 2.9 shows the output spectrum of this device, (a) shows the output of ring and racetrack resonator themselves, and (b) shows the output of the whole device. It can be seen that the whole output is most powerful at the wavelength where the two resonators both generate peaks, which are at 1385 nm and 1660

nm in the figure, and the peaks around them become weak gradually. The reason the peaks around 1385 nm become weak more faster than peaks between 1660 nm is that the two resonators generate peaks with higher q factor at that range. The peaks in whole output have the lowest power where the peaks of the two resonators distribute most separately, which is around 1500 nm.

This design does not require a high-resolution spectrometer, but since the distances between peaks (FSR) in the whole output is pretty large, it is still able to distinguish each peak.

Let's analyze how the existence of particles will impact on the output of the device. First, we place 9 Si particles with a diameter of 100 nm close to the ring resonator. These particles will cause a red shift of the output of ring resonator, which results in the dispersion of the peak generated by the ring and the peak generated by racetrack at 1660 nm, and the overlap of peaks at 1620 nm. In the other word, the shift caused by these particles is one difference of the two FSRs of two resonators. Fig 2.10 (a) shows the whole output of the device in this

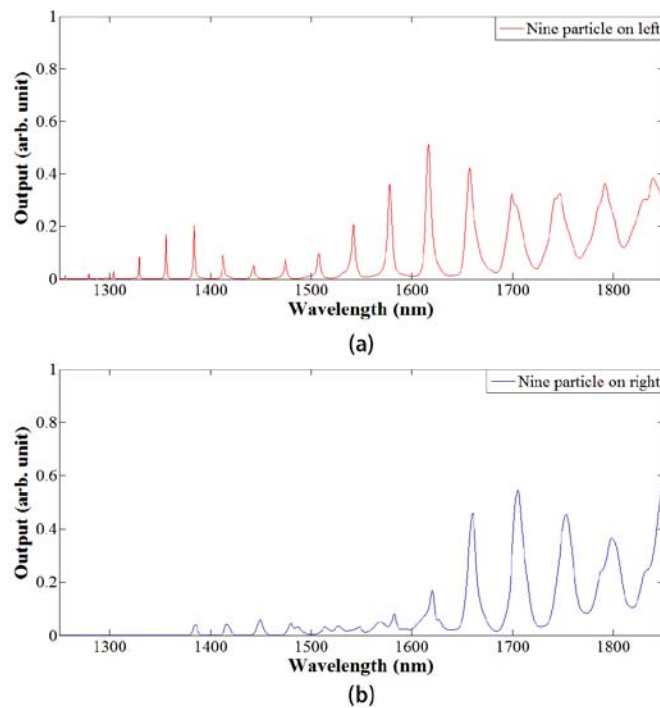


Fig. 2.10. Output of the device when nine Si particles exist close to (a) ring resonator on left, (b) racetrack resonator on right.

simulation. It can be seen that the most powerful peak becomes the peak at 1620 nm instead of 1660 nm. In this condition, we can refer this phenomenon as the highest peak shift from 1660 nm to 1620 nm. However, the shift of output of ring resonator caused by the nine Si particles is only one difference of the two FSRs, which is about 2 nm. This design amplifies this shift of 2 nm to a much larger shift of 40 nm (although the two highest peaks are not generated by the same peaks of each resonator). Thus, by using this design, we do not have to detect the shift of peaks in the accuracy of 0.1 nanometer or even lower, and we do not require a high-resolution spectrometer anymore.

From Fig 2.10 (a) we can find, the ring resonator has a relative small free spectral range (FSR), so a red shift of its output will cause a blue shift of the whole output (1660 nm to 1620 nm).

To the opposite, if the output ring resonator does not shift, but the output of racetrack resonator red shifts a little, the whole output will show a red shift (1660 nm to 1700 nm), as what is shown in Fig 2.10 (b).

On the other hand, if we use metallic particles (for example, Au) to replace the dielectric particles (Si), we will gain similar but exactly opposite results. If Au particles exist close to ring resonator, the effective refractive index of ring waveguide will decrease, which results in a blue shift of its output, and what's shown in the whole output would be a red shift, this effect is similar to that of Si particles exist close to the racetrack. Moreover, to the opposite, the effect when Au particles exist close to racetrack resonator will be similar to that of Si particles exist close to ring resonator.

Therefore, when this new design is applied, in the base that we already made two assumptions of only one type of particles will appear and the particles will affect only one resonator, we still need to make one more assumption that the type of existed particles is already known. Thus, by tracking the shift of the highest peak in whole output spectrum, we can easily find out which resonator is affected by particles.

The description above is for the conditions that the shift of ring or racetrack resonator is exactly one difference of their FSRs. Moreover, then let's discuss what will happen when they do have a shift, but not as much as one difference of the FSRs.

Let's use three Si particles as an example; Fig 2.11 shows the results of this simulation. In Fig (a), three Si particles are placed close to the ring resonator. It can be seen that the highest peak in the whole output is still at 1660 nm. However, the intensity of the two peaks right adjacent is different. In Fig 2.9 (b), when there are no particles, the intensity of these two peaks is similar, but the peak at 1620 is a little lower than 1700nm. As a comparison, the relationship between the intensity of those two peaks is changed in both the two figures in Fig 2.11. In Fig 2.11 (a), the peak at 1620 nm is obviously higher than it in Fig 2.9. (b), and the peak at 1700 nm is a little lower; this phenomenon corresponds to a red shift of the ring resonator, which tells us the particles are located close to ring. Moreover, in Fig 2.11 (b), the peak at 1700 nm is even higher, and the peak at 1620 nm is lower a little bit, this corresponds to a red shift of racetrack resonator.

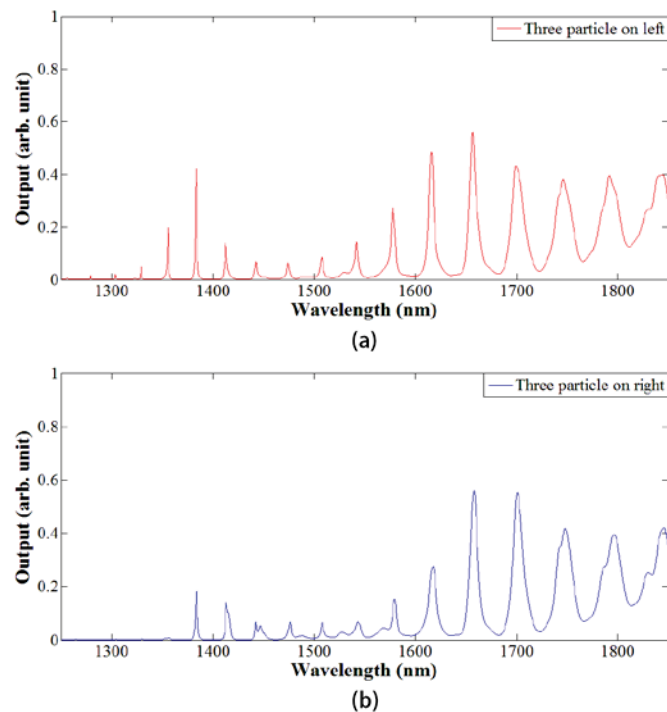


Fig. 2.11. Output of the device when three Si particles exist close to (a) ring resonator on left, (b) racetrack resonator on right.

In summary, when the shift of one resonator is not as much as one difference between the two FSRs, the highest peak in whole output may not shift, but by observing the intensity ratio of the two peaks right adjacent to the highest peak, we can still figure out which resonator is affected. In the condition that dielectric particles exist, the elevation of larger wavelength peak means the shift of racetrack resonator, and the elevation of shorter wavelength peak means the shift of ring resonator. It is certainly that the results will be exactly the opposite when the particles are metallic. Also, for the same reason which described before, this new design still has the function of self-referencing.

### **2.3 Conclusion**

This chapter introduces a design of particle position sensor based on ring resonators. In the basic design, we assume only one type of the particles exist (metallic or dielectric), and they affect only one resonator, then by tracking the shift of each peak, we can figure out the type and position of the particles. Also, if we want to reduce the cost of the device, an improved design based on cascaded double ring resonator is proposed. This design can significantly reduce the requirement of high-resolution spectrometer, as a tradeoff, an extra assumption that the type of particles is known is needed.

## Chapter III

### Plasmonic hydrogen sensor based on integrated micro ring resonator

#### 3.1 Introduction

In the past few decades, the hydrogen sensor has gained the attention of the worldwide scientific community due to its superior characteristics and properties for managing one of the most promising fuels of the future. At present, hydrogen sensors are widely utilized in solid oxide fuel cells, hydrogen transportation, hydrogen storage, and other applications.

Hydrogen is an invisible, flammable, odorless, and highly explosive gas. As a result, a hydrogen sensor is very different from a conventional gas detector. Various types of hydrogen sensors have been developed recently that use very different mechanisms to detect the hydrogen gas; these are briefly summarized in the following:

*Catalytic and metal oxide sensors:* Both of these sensors work on the principle of the reaction of oxygen with combustible gas on the sensor producing heat. These sensors require oxygen as a catalyst, which could get contaminated and become inactive. Thus, the presence of oxygen is essential. Also, these sensors become inactive and poisonous due to contamination. Prolonged exposure of these sensors to combustible gas reduces their performance, and recalibration is necessary.

*Electrochemical sensor:* This is a successful commercial sensor due to its simple operation and high sensitivity. It consists of anode, cathode, and electrolyte. To detect hydrogen, a specific electrochemical reaction takes place between the anode and the cathode, which results in either voltage or current signal in an external circuit.

*Thermoelectric gas sensor:* This sensor works by measuring the heat produced by the reaction between metal catalysts using Cu-Bi thermopiles. The basic principle of this sensor

is based on gas absorption; due to this reason, this technique slows down the recovery and response times.

*Work function based sensor:* This type of sensor includes a metal-insulator-semiconductor transistor and a metal-insulator-semiconductor capacitor. In these sensors, a hydrogen-sensitive catalytic metal layer is deposited on an oxide layer, with the oxide layer deposited on a semiconductor substrate. Thus, diffusion of hydrogen atoms takes place through the metal, and hydrogen gets adsorbed at the interface between the metal and the oxide layer. At the interface, the polarization of hydrogen atoms takes place, which gives rise to a dipole layer and thus a change in voltage.

*Fiber Bragg grating sensor:* This sensor has a fast response and high accuracy and sensitivity, based on doping of  $WO_3$  with a Pt layer where hydrogen gas undergoes an exothermic reaction. Except for the fiber optical sensor, most of the above hydrogen sensors have short life spans due to electrical corrosion. Some of them are dangerous when used in flammable environments due to spark generation. Most of these drawbacks for the sensors mentioned above are overcome by the fiber optical sensor, but this sensor lacks integration ability due to its relatively large volume size.

In this chapter, an on-chip silicon-based micro ring resonator hydrogen sensor is proposed. This sensor could overcome many of the drawbacks of current sensors and have an ultra-small size with easy integration ability and high sensitivity. Also, hydrogen-sensitive materials like Pd and Pt have good adhesion toward the silicon ring resonator. This type of ultra-small optical sensor is environmentally friendly and can perform in harsh and flammable environments.

Hydrogen sensor materials need to meet three basic requirements-sensitivity, selectivity and specificity-which can be found in palladium (Pd) and platinum (Pt). Both Pd and Pt are suitable materials to sense hydrogen because they react with hydrogen to form Pd/Pt hydride.

In this work, we have demonstrated numerically a novel hydrogen sensor based on a micro ring resonator with low concentration detection capability (0~1%) and ultra-small size



( $4 \times 4 \text{ } \mu\text{m}^2$ ), as illustrated in Fig 3.1(a), with a hydrogen-sensitive Pd or Pt metallic layer integrated within the inner layer of the micro ring resonator to have surface plasmon modes excited at the interface. We have compared the performance between Pd- and Pt- layer- based micro ring resonator sensors. We have also studied the Pd/Pt metal layer coverage within the ring resonator, as a heavier Pd/Pt layer will lead to more resonance wavelength shift while it also induces quality factor (Q-factor) degradation due to the loss of part of the metals. Finally, we have also investigated how the width of the Pd/Pt layer will affect the performance of this type of optical sensor and revealed the relationship between the minimum feature width and

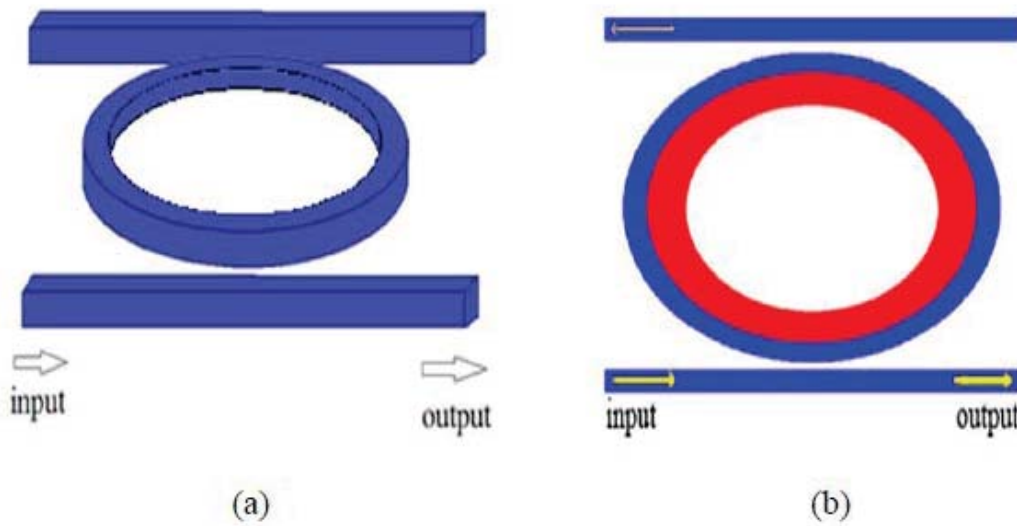


Fig. 3.1 (a) The 3D basic micro ring resonator structure, coupled with straight waveguides. (b) Top view of the hydrogen-sensitive materials Pd/Pt layer coating the ring resonator. The blue part represents the Si ring waveguide, and the red part represents the hydrogen-sensitive Pd/Pt layer

the evanescent wave of the ring waveguide mode.

### 3.2 Basic model and simulation

#### 3.2.1 Model and simulation results

The basic model in our simulation is shown in fig 3.1 (b). The micro ring resonator is evanescently coupled with the straight waveguide, and the diameter of the micro ring is 3000 nm. The light is injected into the input port and collected at the output port of the slab

waveguide, which has a width of 200 nm, to keep the single waveguided mode condition. The gap between the slab waveguide and the micro ring resonator is 100 nm, the power coupled out depends not only the round trip ring loss, but also on the coupling gap, and we choose the 100 nm coupling gap as it is very close to the critical coupling condition without Pd/Pt coating. In fig 3.1 (b), the layer in red is a layer of hydrogen-sensitive material (Pd/Pt) of width 400 nm deposited on the inner surface of the ring resonator.

The core materials of the micro ring resonator in the FDTD simulation are silicon. For the slab waveguide and the micro ring resonator, the refractive index of Si, 3.48 at wavelength 1550 nm, is used; the bottom cladding is SiO<sub>2</sub> with refractive index 1.45.

First, take palladium as an example: if the concentration of hydrogen in the surrounding environment increases, the palladium will form palladium hydride, and the  $n_{\text{eff}}$  will change according to the change in the refractive index of the palladium layer. The refractive index of pure palladium, at wavelength 1550 nm, is  $n = 3.164$ ,  $a = 665790/\text{cm}$ , where  $n$  is the real part and  $a$  is the imaginary part of the refractive index. Both the real and the imaginary parts of the refractive index will vary according to the change in the concentration of hydrogen in the surrounding environment.

According to the measurement of the refractive index of palladium hydride, both the real

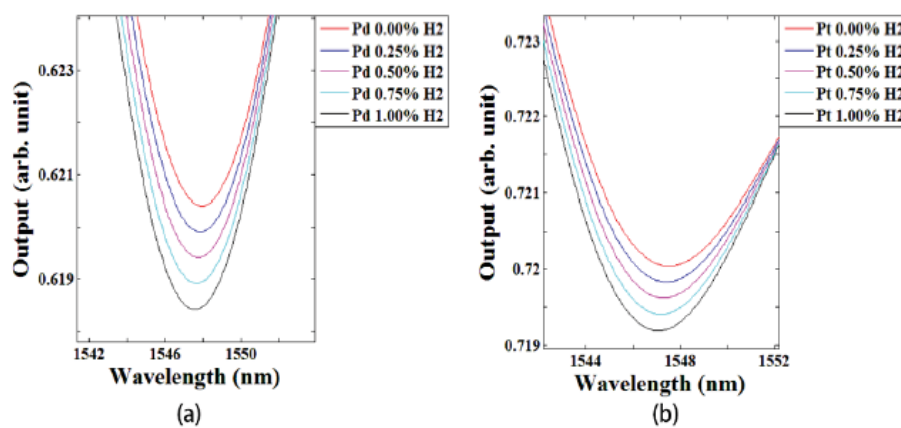


Fig. 3.2 Resonance wavelength shift and relative intensity change of the fully covered ring resonator hydrogen sensor with hydrogen concentration variation from 0~1%. (a) Pd-coated structure. (b) Pt-coated structure

and the imaginary parts of the refractive index change when the concentration of the hydrogen gas varies from 0% to 1%. In this range, the change of the refractive index of palladium hydride is almost linear to the variation in the hydrogen concentration.

For thin palladium film at light wavelength 1550 nm, when hydrogen concentration is increased, for example, from 0% to 1%, the real part of the refractive index is decreased, and the imaginary part is increased as follows:  $\Delta n = -0.033$  and  $\Delta a = 5432/\text{cm}$ ; for platinum, the corresponding parameters at wavelength 1550 nm are  $n = 5.3678$ ,  $\Delta n = -0.089$ ,  $a = 572890/\text{cm}$ , and  $\Delta a = 14674/\text{cm}$ .

These values of refractive index for Pd and Pt are applied to our FDTD simulation. The perfectly matched layer (PMLs) are used as the boundary condition. The input signal is a sinusoidal pulse with a wavelength range from 1500 nm to 1580 nm and a grid size of 20 nm, and long evolution time steps are used to ensure the precision and resolution of our simulation results.

Fig 3.2 shows the resonance wavelength shift between 1530 and 1560 nm for both Pd- and Pt- coated micro ring resonators when hydrogen concentration is increased from 0% to 1%. A significant resonance wavelength shift and relative intensity change can be observed. Fig 3.2 (a) shows the results for a Pd-coated structure; with a 1% increase of hydrogen concentration, the resonance wavelength has a shift of approximately 0.35 nm (i.e., 1547.9 nm at 0% hydrogen and 1547.55 nm at 1% hydrogen), and the relative intensity decreases from 66.66% to 65.77%, i.e., 0.22% for 1% increase of hydrogen concentration. On the other hand, Fig 3.2 (b) shows the result for a Pt-coated structure, where the resonance wavelength shift and intensity change is about 1.02 nm and 0.18%, respectively, with 1% increase of hydrogen concentration. Compared to the Pd layer, the resonance wavelength shift is noticeably larger using Pt for the same variation in hydrogen concentration. From the above results, the integrated micro ring resonator hydrogen sensor can detect very small changes in hydrogen concentration; the resonance wavelength change is at least one order of magnitude larger than the optical fiber-based hydrogen sensor, which is due to the ultra-small size of the micro ring resonator structure.

Fig 3.3 shows the relationship between the resonance wavelength shift/intensity change and the hydrogen concentration variation for both Pd- and Pt- coated layers. Fig 3.3 (a) shows that for 1% change in hydrogen concentration, the Pt- coated microring resonator has about three times higher amplitude of resonance wavelength shift than the Pd- coated structure,

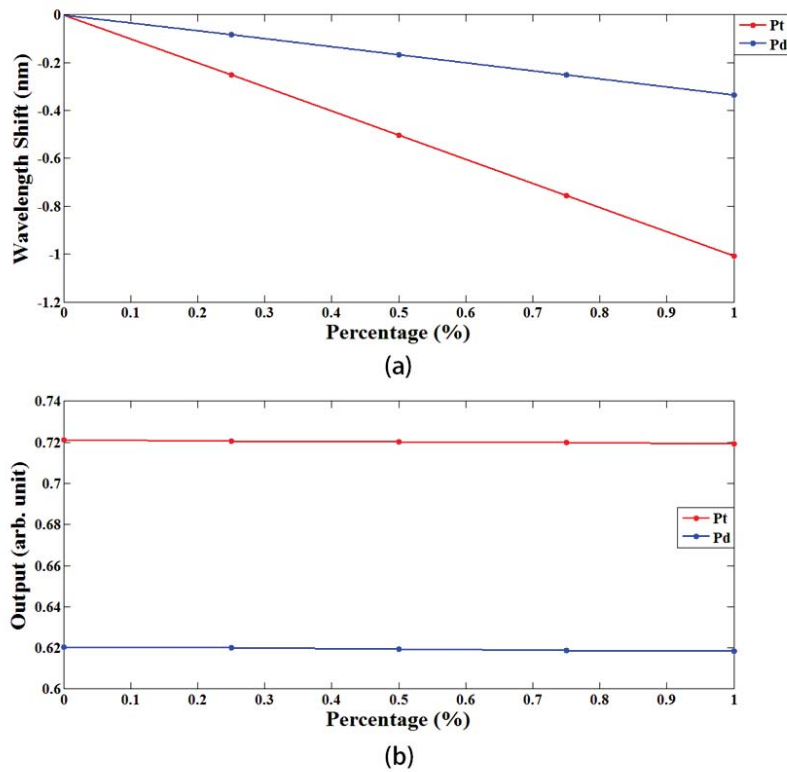


Fig. 3.3 The comparison between Pd- and Pt- coated structures. (a) Resonance wavelength shift. (b) Relative intensity change.

which is from the larger variation of the real part of the Pt refractive index with the change of the hydrogen concentration. While Fig 3.3 (b) shows that the change of the resonance intensity is almost the same for both the Pd- and Pt- coated structures, even  $\Delta a$  is larger for Pt. The lower resonance intensity for the Pd layer is due to the higher optical loss, which is reflected in the relatively larger value of the imaginary part of the Pd refractive index.

### 3.2.2 Investigation of the coverage proportion of Pd/Pt layer

For the hydrogen sensitive materials, both Pd and Pt have a significant imaginary part of the refractive index at a wavelength around 1550 nm, which means they will introduce a

certain amount of loss in the ring resonator and induce a degradation of the resonance mode quality factor (Q factor). Meanwhile, the real part of the refractive index determines the shift

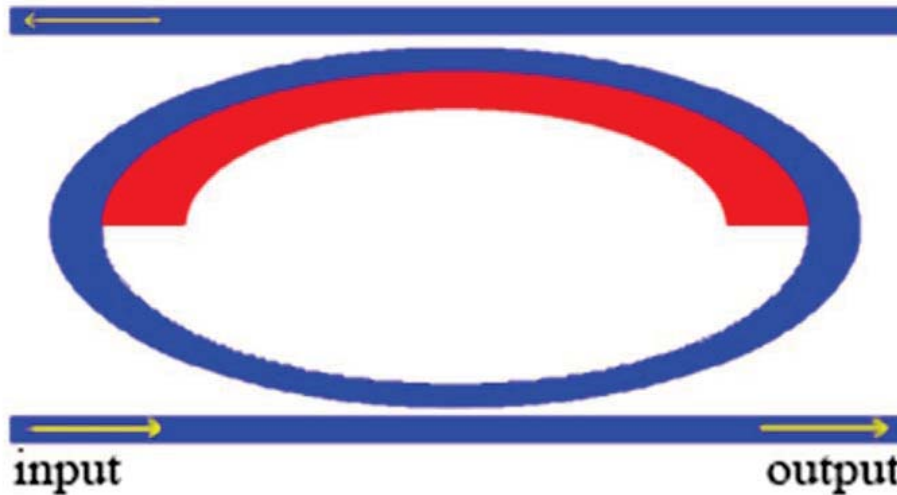


Fig. 3.4 Top view of the ring resonator with partial coverage of hydrogen sensitive material Pd/Pt layer.

in resonance wavelength with the change in hydrogen concentration. It can be clearly seen that there is a tradeoff between the resonance wavelength shift and the Q degradation, i.e., with more coating of the Pd/Pt layer, there should be more induced resonance wavelength shift while at the same time there is more Q degradation. Therefore, two important parameters, the cover proportion of Pd/Pt layer of the micro ring resonator and the width of Pd/Pt layer, are interesting to investigate further.

Cover proportion is investigated first. Simulation is done with three different structures, i.e., the micro ring resonator is (1) one-fourth, (2) half, and (3) three-fourths covered with the hydrogen-sensitive material Pd/Pt layer, and is compared with the above results with a fully covered structure. As an example, Fig 3.4 illustrates the micro ring resonator structure with the Pd/Pt layer half covered.

Fig 3.5, Fig 3.6, and Fig 3.7 show the simulation results of one-fourth, half, and three-fourths Pd/Pt layer covered micro ring resonator structure, respectively. With 1% increase of hydrogen concentration, the resonance wavelength shift and relative intensity

change for Pd are 0.08 nm, and 0.47% for the one-fourth covered structure, 0.155 nm and 0.465% for the half covered structure, and 0.30 nm and 0.21% for the three-fourths covered structure. As described above, the results for the fully covered structure are 0.35 nm and 0.22%. The corresponding results for the Pt-based structure are 0.11 nm and 0.92% for the one-fourth covered structure, 0.31 nm and 0.59% for the half covered structure, 0.62 nm and 0.30% for the three-fourths covered structure, and 1.02 nm and 0.18% for the fully covered structure.

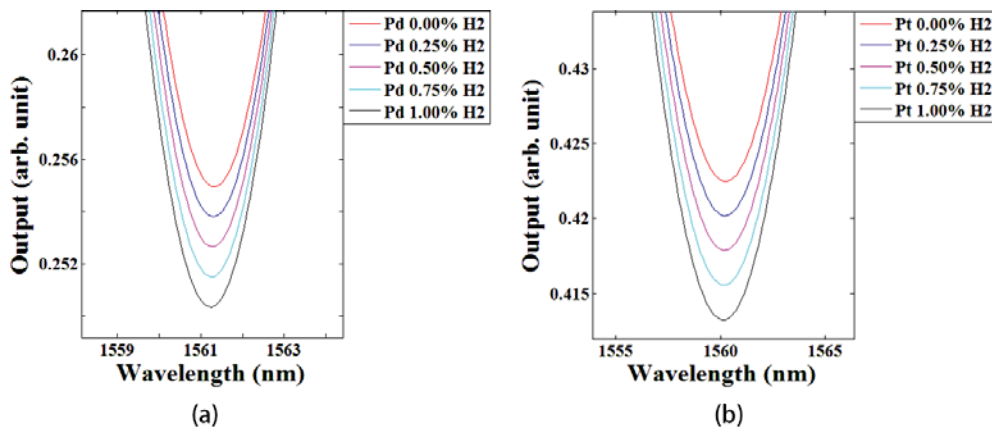


Fig. 3.5 Results of the one-fourth covered ring resonator hydrogen sensor. (a) Pd-coated structure. (b) Pt-coated structure.

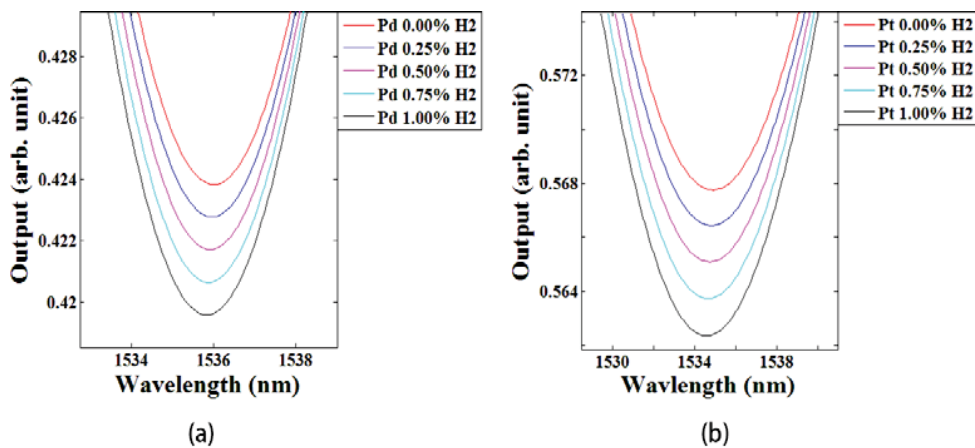


Fig. 3.6 Results of the half covered ring resonator hydrogen sensor. (a) Pd-coated structure. (b) Pt-coated structure.

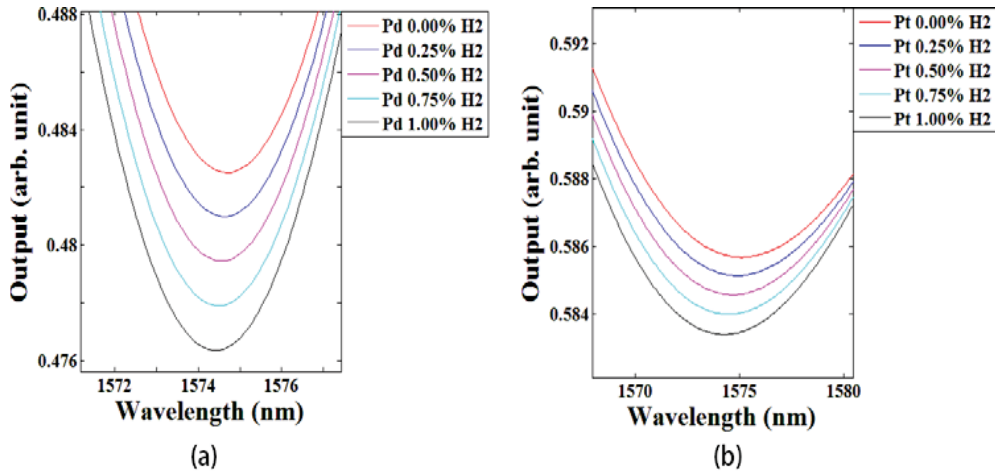


Fig. 3.7 Results of the three-fourths covered ring resonator hydrogen sensor. (a) Pd-coated structure. (b) Pt-coated structure.

It can be clearly observed that a higher coverage proportion would contribute to a larger resonance wavelength shift. As illustrated in Fig 3.8, taking the Pt layer as an example, the Q-factor of the resonance mode for a larger coverage portion degrades only slightly; it changes from nearly 70 for the one-fourth covered structure to about 50 for the fully covered structure. However, the different coverage proportion causes a significant relative intensity difference between the resonance mode peak and bottom. Note that results for the Pt- covered structure at 1% hydrogen concentration are used in Fig 3.8. The relative intensity difference for Pt structure is 3.03%, 8.09%, 16.4%, and 37.69% for fully, three-fourths, half, and

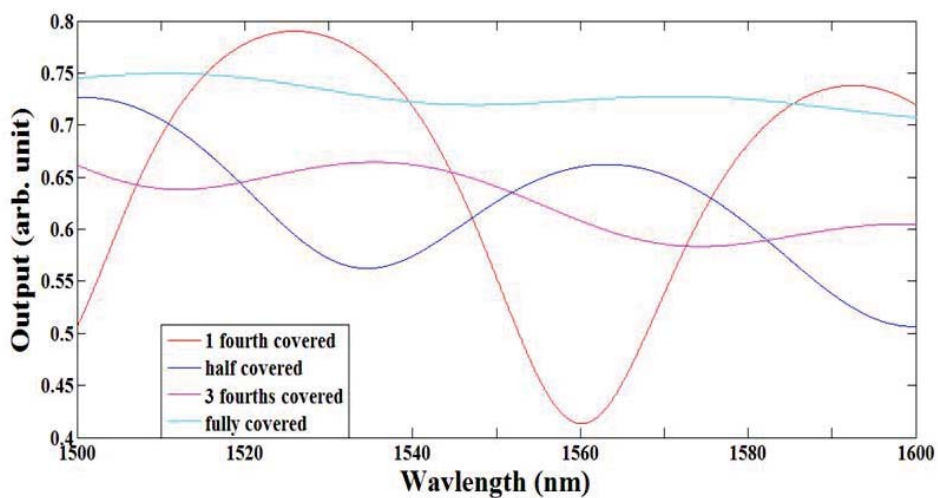


Fig. 3.8 The comparison of spectrum shape between different coverage proportions for the Pt-covered structure at 1% hydrogen concentration.

one-fourth covered structure, respectively. While for Pd layer, the corresponding results are 10.55%, 20.14%, 33.30%, and 55.57%. The results from Fig 3.5 to Fig 3.8 clearly demonstrate the tradeoffs among different coverage proportions of Pd/Pt layers.

### 3.2.3 Investigation of the width of Pd/Pt layer

Another important parameter, i.e., the width of the Pd/Pt layer, which will also affect the resonance wavelength shift, Q-factor, and relative intensity difference, is also studied in this section.

Compared to the 400 nm Pd/Pt layer width, we select a half-covered structure and a 100 nm Pd/ Pt layer width to investigate this parameter, because it suffices for observing how the

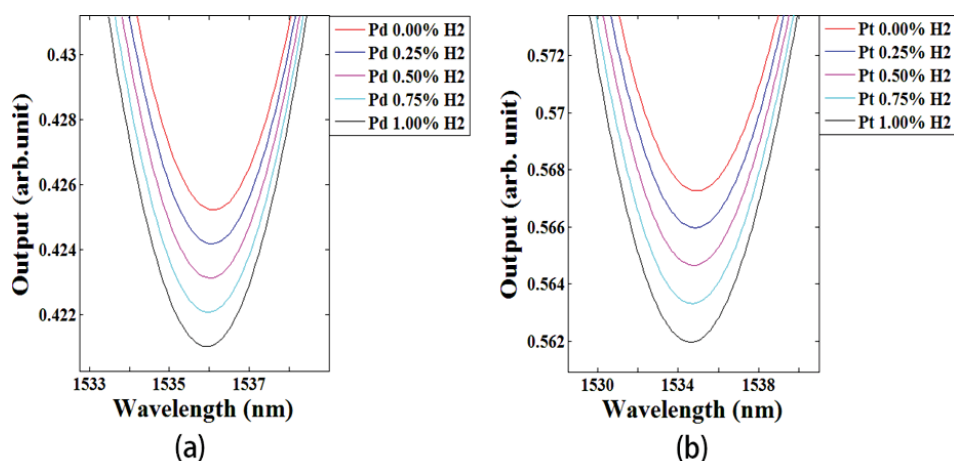


Fig. 3.9 Results of the ring resonator hydrogen sensor with the width of sensitive material layer 100 nm. (a) Pd-coated structure. (b) Pt-coated structure.

evanescent field of the ring waveguide mode penetrates into the Pd/Pt coated layer to understand how the width of the Pt layer will impact the ring resonator sensor.

The resonance wavelength shift and the relative intensity change are illustrated in Fig 3.9, which shows the results for a ring resonator device coated with a 100 nm width hydrogen-sensitive material Pd/Pt layer. The resonance wavelength shift and relative intensity change for the Pd structure are 0.18 nm and 0.44% for 1% hydrogen concentration increase, and for Pd, they are 0.31 nm and 0.55%, respectively. These values are almost equal to the corresponding results of the 400 nm width Pd/Pt layer structure, as illustrated in the above sections. These results tell us that the width of the hydrogen-sensitive material Pd/Pt layer has



no significant impact on the performance of the device, at least the Pd/Pt layer thickness is

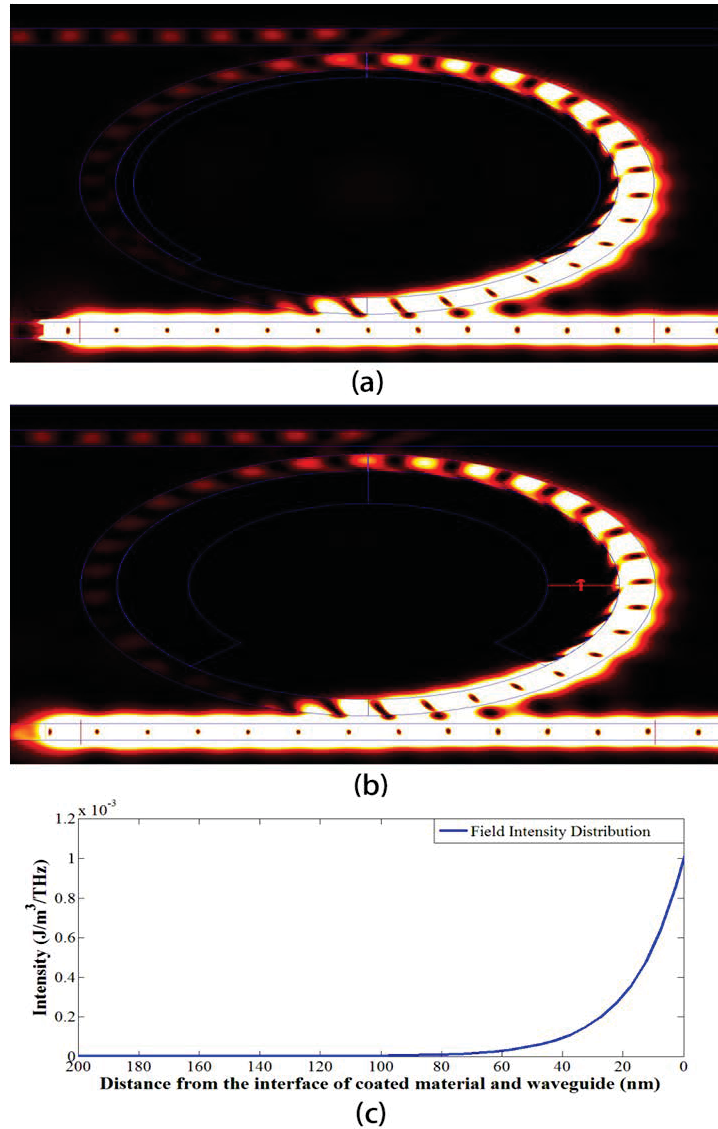


Fig. 3.10 Electromagnetic field intensity distribution at resonance wavelength 1535 nm for Pt layer structure. (a) for 100 nm width, (b) for 400 nm width, (c) EM field intensity along the red line shown in (b)

more than 100 nm.

The electromagnetic (EM) field distribution can explain this phenomenon more clearly. We apply a continuous wave at the resonance wavelength (1535 nm) for both 400 and 100 nm width Pt layer structures, and the electromagnetic field intensity distributions are shown in Fig 3.10. Pt with 0% hydrogen concentration is used as an example in this simulation. Note

that in Fig 3.10 (a) and (b), the brightness represents the intensity of the EM wave.

We can observe that when the EM wave enters into the ring resonator from the waveguide, the evanescent wave of the ring resonator waveguide begins to penetrate into the Pt-coated layer. It is worth noting that the penetration depth of the evanescent field into the Pt layer is about the same for both the 100 nm and 400 nm Pt layer width, which, from Fig 3.10, is about 60 nm. So a 100 nm width Pt layer is adequate to feel the largest part of the EM field. This is the reason that there is no significant difference between the performances of the two different Pt-layer width structures of 100 nm and 400 nm. Fig 3.10 (c) shows the EM field intensity along the red line in (b); the horizontal axis is the distance in nanometers from the interface of the Pt layer and the Si layer. It can be seen that the EM field has an exponential decay in intensity and becomes almost zero close to 100nm, which is a typical characteristic of the surface plasmon modes excited by the ring resonator waveguide. So regarding device fabrication, this study should provide us a route to balance the challenges in small Pd/Pt layer width fabrication, while at the same time to ensuring enough Pd/Pt layer width to optically interact with the micro ring resonator's evanescent field. For the hydrogen detection limit, we have tried very low hydrogen concentration; within our simulation model, as low as 0.12% hydrogen concentration can be resolved using our silicon-based ring resonator, this is comparable or even lower than most of existing hydrogen sensors; compared to the optical fiber based hydrogen sensor, the wavelength shift is larger, while the Q is lower. The sensitivity is 1.02 nm for 1% hydrogen for Pt and 0.35 for Pd, respectively.

### **3.3 Conclusion**

In summary, this chapter has proposed and numerically demonstrated an ultra-small plasmonic hydrogen sensor based on an integrated micro ring resonator coated with a hydrogen-sensitive palladium/platinum layer. The device is very sensitive to low hydrogen concentration variation (0~1%), with nm resonance wavelength shift due to the excitation of plasmonic modes, which is at least an order of magnitude higher than the fiber-based optical hydrogen sensor. We have also investigated the tradeoff between the portion coverage of the palladium/platinum feature width is determined to be the length of the ring waveguide

evanescent wave. The ultra-small size of the plasmonic hydrogen sensor ( $4 \times 4 \text{ } \mu\text{m}^2$ ) will have the potential to be applied in integrated optical circuits with large integration capability and portability.

## Chapter IV

### High-Contrast Sub-wavelength Grating Structure for Wideband Reflector at Visible Light

This chapter introduces an attempt to design a wideband reflector at visible light wavelength range based on the high-contrast sub-wavelength grating structure with the possibility to fabricate easily. However, due to there are no significant results, this chapter is going to just briefly introduce the high contrast grating (HCG) structure and state the results.

#### 4.1 Introduction of HCG structure

Optical gratings are among the most fundamental building blocks in optics. They are well understood in two regimes: the diffraction regime, where the grating period is greater than the wavelength and the deep-subwavelength regime, where the grating period is much less than the wavelength. However, between these two well-known regimes lies a third, relatively unexplored regime: the near-wavelength regime, herein defined as a grating whose period is between the wavelengths inside the grating material and its surrounding media. In

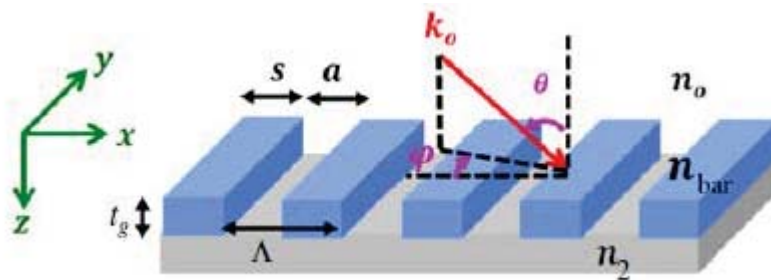


Fig. 4.1. Generic HCG structure. The grating comprises simple dielectric bars with high refractive index  $n_{bar}$ , surrounded by a low-index medium  $n_0$ . A second low-index material  $n_2$  is beneath the bars. The plane wave is incident from the top at an oblique angle.  $\Lambda$ , HCG period;  $s$ , bar width;  $a$ , air gap width;  $t_g$ , HCG thickness. For surface-normal ( $\theta = 0$ ) TE incidence,  $\varphi = 0$ , and the electrical field is parallel to the grating bars; whereas for TM,  $\varphi = \pi/2$ , and the electrical field is perpendicular to the grating bars.

this regime, gratings behave radically differently and exhibit features that are not commonly attributed to gratings.

Fig 4.1 shows the schematic of a generic HCG, with air as the low-index medium on top and between the grating bars, a second low-index material beneath the bars, and an incident plane wave at an oblique angle. Several important parameters of subwavelength grating structure are introduced here such as the period  $\Lambda$ , grating width  $s$  (or which can refer to the fill factor equal to the ratio of grating width to the period), and grating height  $t_g$ .

The HCG is polarization sensitive by its nature of one-dimensional (1-D) periodicity. Incident beams with  $E$ -field polarization along and perpendicular to the grating bars are referred to as transverse electric (TE) and transverse magnetic (TM) polarizations, respectively. We also show two incident characteristic angles,  $\theta$  and  $\varphi$ , the incident directions between the incident beam and the  $y$ - $z$  and the  $x$ - $z$  planes, respectively.

By fully surrounding the high-index medium with low-index materials (this is which the HCG refers to), many unexpected, extraordinary features were obtained by scientists. One of these features is an ultra broadband (at wavelength range approximately from 1400 nm-2100 nm) high reflectivity ( $> 99\%$ ). Another feature is a high-quality-factor resonance ( $Q > 10^7$ ). Both features are surprising because they far exceed what was observed in other subwavelength gratings, which were etched on a high-index substrate without the additional index contrast at the exiting plane.

## 4.2 The attempt of wideband reflector at visible light range

The wideband reflector based on the subwavelength grating structure for both zero-contrast grating (ZCG) and high-contrast grating (HCG) working on telecommunication wavelength range (around 1550 nm) has been attracted the attention of scientists for many years, due to its great potential application in the communication industry. However, if we use the same mechanism to design a similar reflector working at visible light range (400-760 nm), and utilize the common material  $Si_3N_4$  as the gratings, then a result turns out that the refractive index of substrate material must be approximately equal to 1, which is air. This

makes a big difficulty in fabrication processes. So our goal in this project is to find easily fabricated visible range wideband reflector. We select  $Si_3N_4$ , which contains a relative high refractive index ( $\approx 2.00$ ) among common materials which are transparent (no absorption) in visible range, as gratings; and  $SiO_2$ , which is glass, with refractive of approximately 1.46 at visible range, as substrate. With one more limitation that the height of gratings  $t_g$ , shouldn't be higher than twice the width of the gratings  $s$ , the difficulty of the fabrication of this device is already controlled to be as low as we want.

In simulation, we set the incident light to be normal to the grating structure surface, and collected data for structures with the above-stated configuration and following variables: period from 100 nm - 700 nm with per 100 nm a step; fill factor from 0.3 - 0.7 with per 0.1 a step; and grating height from 100 nm to 600 nm with per 100 nm a step. Thus, 129 HCG structures with different parameters are simulated.

However, we did not find any results which even is just possibly trended to a wideband reflector in the visible range. The results turns out that the refractive difference between  $Si_3N_4$  (2.00) and  $SiO_2$  (1.46) is too low to build a HCG subwavelength grating structure which could form a resonance cavity results in a wideband reflection in visible range.

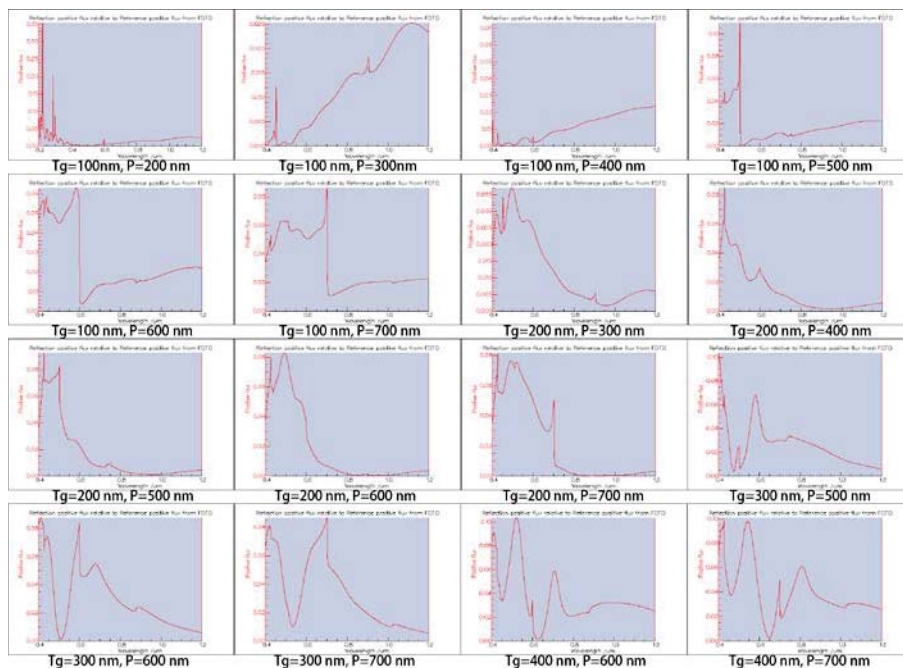


Fig. 4.2. Results of structures with fill factor of 0.3

Here the results for a fill factor of 0.3 is shown in Fig 4.2 as examples. Because of the non-significance, the rest of results will not be shown here.

This attempt does not turn to any significant results. However, the huge number of HCG structures simulated is a great value to us, the results will be helpful for further investigations related with subwavelength grating structures.

## **Chapter Five Introduction of Finite Difference Time Domain (FDTD) method in Electromagnetism**

### **5.1 Introduction**

Many areas of modern technologies are deeply relative to electromagnetic (EM) field, especially the high-frequency EM field. The analysis and calculation of complicated high-frequency EM system and the integration of high-frequency EM field and complicated objectives have become a type of important topics regarding the development of modern technologies. In many fields such as telecommunication, radar, substance detection, EM protection, EM compatibility, medical diagnosis, strategic defense, and many other areas in agricultural & industrial production and daily life, the problems of high frequency EM field including its propagation, radiation, scattering, and penetration, are all playing an important role.

The ultimate request in solving the EM field problems is finding out an analytical solution which accurately fulfills Maxwell's equations. However, only some typical geometry shapes and problems with simple structures are possible for us to solve analytically. On the other hand, a main feature of high-frequency EM field problems in modern electromagnetism is the high complexity. Despite many analytical solutions of classic problems are still helpful for us to deeper understand the electromagnetism, they are more likely to be useless for solving the real engineering projects.

Modern EM systems are usually working in an extremely complicated environment, and the objectives that EM wave interact with always have complicated shape and structure. For example, some EM systems are used in objectives such as airplanes, rockets, and ships, and themselves as EM wave also become a more complicated EM scattering system combining with these objectives. Their complexity shows not only in their configurations but also in



materials which are consist of these devices. A complicated EM system usually contains several types of complicated EM physical processes. Thus the configuration of the system has an intensive impact on its EM features.

In this condition, the simple EM models are way behind to fit the requirements of modern EM field engineering, we have to consider many complicated factors in real condition, and this is an extremely hard work. To satisfy the requirement of solving the endlessly complicated problems in electromagnetic engineering, many powerful new methods of EM field problem are emerging and developing. Among them, those numerical methods are the only ones which can be widely applied. Since the 1960s, there are several numerical calculation methods are developed. As one of them, the differential form based Finite Difference Time Domain (FDTD) method has a very wide application range. This method remains the time variables in Maxwell's vorticity equations and applies the equations in the time-space domain without transformation. It can offer the homogeneous (instantly) and non-homogeneous (steady state) solution of equations. It repeatedly runs the finite difference form equation which directly comes from Maxwell's vorticity equations and thus realizes the simulation of the propagation of wave and the interaction between wave and objectives in the digital space in computers. The main disadvantage of this method is that the computational area covers not only the structure surface but also the inner space and sufficient outer space, so as to effectively satisfies the radiation condition. However, since it is based on the most common Maxwell's equations, it has a very wide application range.

In 1966, Kane S. Yee proposed a simulation method in his famous article "*Numerical Solution of Initial Boundary Value Problems Involving Maxwell's Equation in Isotropic Media,*" which is latterly called Finite Difference Time Domain (FDTD) method. He utilized the spatial discretion method which is called the Yee Lattice latterly to transform Maxwell's vorticity equations into differential form and successfully simulated the interaction between EM pulse and ideal conductor. Certainly, in recent view, this method is still a simple model when Yee initially proposed it. Many scientists spent nearly twenty years to develop and finally made it becomes mature. However, the basic theory of FDTD method is not the

focusing point of this thesis, so only the Yee Lattice, and the differential form of Maxwell's vorticity equations are going to be introduced, the other details which are improved by later scholars will not be stated.

## 5.2 Yee Lattice

The phenomenon of EM field is governed by Maxwell's equations, and their general form is vorticity equations based on time variables. Thus, to construct a time domain numerical method for EM field based on them are certainly.

In general, the time domain calculation of EM field has to be operated in a 4-dimensional space including time. If we want to utilize finite difference method, we first need to discretize the variable space of the problem, that is to construct suitable lattice system. When we construct the lattice for Maxwell's equations, we have to face the difficulty not only of in 4-dimensional space but also of simultaneously compute the six components of the electrical and magnetic field. How to reasonably discretize the six unknown field components becomes essential to construct a high accurate differential form. It is because of proposing a reasonable lattice system that Yee could successfully build up the FDTD method. We call the lattice he proposed Yee Lattice, in the Cartesian coordinate system it is shown in Fig 5.1.

This lattice takes values of the electrical field and magnetic field crossly in the space.

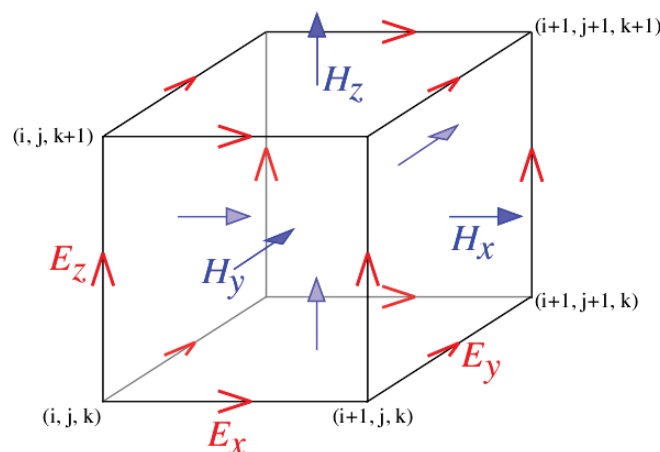


Fig. 5.1 Yee Lattice of FDTD method in electromagnetism

Thus every electrical component in every coordinate flat are surrounded by four magnetic

components around it, and vice versa. This EM field configuration in space meets the basic law - Faraday's law of induction and Ampere's circuital law, that is, the basic requirement of Maxwell's equations, and thus this configuration can simulate the spatial propagation of EM wave. It is because of this lattice system, the FDTD method of electromagnetism becomes a reality.

The computation of EM field has a deep relationship with the EM property of spatial media so that besides the discrete points of EM field, we also have to know the EM parameters of medium for every discrete points, including the permittivity and conductivity, as well as the permeability and the equivalent magnetoresistance. By offering different EM parameters to different points in the lattice, the FDTD method becomes able to simulate the interaction between EM wave and various complicated structure. Of course, applying cubic model on curved geometry surface will cause some problem in accuracy, but it could be overcome by utilizing other shapes of the lattice.

In Yee Lattice, the distance between each field components in every direction is half one grid. Thus the distance between each same kind of components (E or H) is one grid. The lattice in Fig 5.1 doesn't give the discretion method of the time. To ensure the computation accuracy, the time grid size (or we call the time step length) has to satisfy some relationship with spatial grid size. Indeed, the time step length could be selected as a half of the time required for EM wave to propagate one spatial grid size. Therefore, once we determine the spatial grid size while using FDTD method in real, the time step length is also determined.

The statement above just gives the Yee Lattice in Cartesian coordinate system. However, some of the principles are helpful for us to build up lattices with other shapes which can suit different geometrical structures. Because lattices with other shapes are not what we focused in this thesis, only the applying of Cartesian coordinate based Yee Lattice will be introduced.

### **5.3 Maxwell's equations and their finite difference form**

The Maxwell's equations summarize the basic law of EM field in macro; they are consists of two divergence equations and two vorticity equations. The two vorticity equations

are Faraday's law of induction and Ampere's circuital law. In essential, the two vorticity equations are the basic of Maxwell's equations, because the two divergence equations can be derived from them. Therefore, the research of EM field always starts from these two vorticity equations. Moreover, the FDTD method is also like this.

To emphasize the key problem in basic theory, let's make some assumption. Assume that the EM field problem we investigate involving only isotropy, linear, and un-time-related medium, but the loss of electricity and magnetic can exist. Therefore, in a passive area (in where has no EM wave source exists), we can express the two vorticity equations in the following form:

$$\nabla \times \mathbf{E} = -\mu \cdot \frac{\partial \mathbf{H}}{\partial t} - \sigma_m \cdot \mathbf{H}, \quad (5.1a)$$

$$\nabla \times \mathbf{H} = \varepsilon \cdot \frac{\partial \mathbf{E}}{\partial t} + \sigma_e \cdot \mathbf{E}, \quad (5.1b)$$

where  $\mathbf{E}$  is intensity of electrical field, unit in V/m;  $\mathbf{H}$  is intensity of magnetic field, unit in A/m;  $\varepsilon$  is permittivity, unit in F/m; and  $\mu$  is permeability, unit in H/m;  $\sigma_e$  is conductivity, unit in S/m; and  $\sigma_m$  is equivalent magnetoresistance, unit in  $\Omega/m$ . Here we introduce the equivalent magnetoresistance in order to make the equations symmetrical.

To derive the six field components, in Cartesian coordinate system, let  $\mathbf{E} = E_x \cdot a_x + E_y \cdot a_y + E_z \cdot a_z$ ,  $\mathbf{H} = H_x \cdot a_x + H_y \cdot a_y + H_z \cdot a_z$  (where  $a_x$ ,  $a_y$ , and  $a_z$  are the three unit vector in each coordinates), then we can expanse equation (5.1) as following:

$$\frac{\partial E_x}{\partial t} = \frac{1}{\varepsilon} \cdot \left( \frac{\partial H_z}{\partial y} - \frac{\partial H_y}{\partial z} - \sigma_e \cdot E_x \right), \quad (5.2a)$$

$$\frac{\partial E_y}{\partial t} = \frac{1}{\varepsilon} \cdot \left( \frac{\partial H_x}{\partial z} - \frac{\partial H_z}{\partial x} - \sigma_e \cdot E_y \right), \quad (5.2b)$$

$$\frac{\partial E_z}{\partial t} = \frac{1}{\varepsilon} \cdot \left( \frac{\partial H_y}{\partial x} - \frac{\partial H_x}{\partial y} - \sigma_e \cdot E_z \right), \quad (5.2c)$$

$$\frac{\partial H_x}{\partial t} = \frac{1}{\mu} \cdot \left( \frac{\partial E_y}{\partial z} - \frac{\partial E_z}{\partial y} - \sigma_m \cdot H_x \right), \quad (5.3a)$$

$$\frac{\partial H_y}{\partial t} = \frac{1}{\mu} \cdot \left( \frac{\partial E_z}{\partial x} - \frac{\partial E_x}{\partial z} - \sigma_m \cdot H_y \right), \quad (5.3b)$$

$$\frac{\partial H_z}{\partial t} = \frac{1}{\mu} \cdot \left( \frac{\partial E_x}{\partial y} - \frac{\partial E_y}{\partial x} - \sigma_m \cdot H_z \right), \quad (5.3c)$$

The approximate differentiation of Maxwell's vorticity equations is coming from this six first order partial differential equations of each component of EM field. In some special EM field problems, the 3-dimensional problem can be simplified to the 2-dimensional problem, which can significantly reduce the difficulty of the problem.

In scattering problems, if the shape and structure of incident wave and scattering objectives are both not related to z-direction, then the scattering field is not related to z, in this condition, we can solve any cross section that is perpendicular to z direction instead of solving the whole 3-dimensional structure. When the electrical field and magnetic field are both unrelated to z direction, equations (5.2) & (5.3) are separated into two independent groups, of which one's electrical field has only z component, and the other's magnetic field has only z component. We call the one with only  $E_z$  transverse magnetic wave, and the other transverse electrical wave. Their equations are,

TM wave

$$\frac{\partial E_z}{\partial t} = \frac{1}{\varepsilon} \cdot \left( \frac{\partial H_y}{\partial x} - \frac{\partial H_x}{\partial y} - \sigma_e \cdot E_z \right), \quad (5.4a)$$

$$\frac{\partial H_x}{\partial t} = -\frac{1}{\mu} \cdot \left( \frac{\partial E_z}{\partial y} + \sigma_m \cdot H_x \right), \quad (5.4b)$$

$$\frac{\partial H_y}{\partial t} = \frac{1}{\mu} \cdot \left( \frac{\partial E_z}{\partial x} - \sigma_m \cdot H_y \right), \quad (5.4c)$$

TE wave:

$$\frac{\partial H_z}{\partial t} = \frac{1}{\mu} \cdot \left( \frac{\partial E_x}{\partial y} - \frac{\partial E_y}{\partial x} - \sigma_m \cdot H_z \right), \quad (5.5a)$$

$$\frac{\partial E_x}{\partial t} = \frac{1}{\varepsilon} \cdot \left( \frac{\partial H_z}{\partial y} - \sigma_e \cdot E_x \right), \quad (5.5b)$$

$$\frac{\partial E_y}{\partial t} = -\frac{1}{\varepsilon} \cdot \left( \frac{\partial H_z}{\partial x} + \sigma_e \cdot E_y \right), \quad (5.5c)$$

It can be observed from the equations above that, TM wave has only  $E_z$ ,  $H_x$ , and  $H_y$  components, while TE wave has only  $H_z$ ,  $E_x$ , and  $E_y$  components.

Then let's derive the differential form of Maxwell's equations from here. For convenience, we will use the Yee Lattice as shown in Fig 5.1. Let  $\Delta x$ ,  $\Delta y$ , and  $\Delta z$  be the grid size in x, y, and z-direction, the spatial coordinate of grid points can be simply expressed as

$$(i, j, k) = (i\Delta x, j\Delta y, k\Delta z)$$

where  $i, j$ , and  $k$  are all integers, indicate the number of grids of spatial steps. The time step length is expressed by  $\Delta t$ , and letter  $n$  is used to indicate its number. In general, a time dependent parameter is related to spatial coordinate, as well as the time variable. For convenience, we put the time variable at the upper right corner of the sign, and use the following expression:

$$F^n(i, j, k) = F(i\Delta x, j\Delta y, k\Delta z, n\Delta t),$$

where  $F$  can be any time dependent parameter.

In the transformation from Maxwell's vorticity equations to differential equations, Yee utilized second order central difference quotient approximation. In the Yee Lattice, the distance between the field components is a half of spatial grid size, thus the central difference quotient approximation of  $F^n(i, j, k)$  in x direction can be derived:

$$\frac{\partial F^n(i, j, k)}{\partial x} = \frac{F^n(i+\frac{1}{2}, j, k) - F^n(i-\frac{1}{2}, j, k)}{\Delta x} + O(\Delta x^2), \quad (5.6)$$

Similarly, the central difference quotient approximation of time is also gained by calculating every half of the time step length:

$$\frac{\partial F^n(i, j, k)}{\partial t} = \frac{F^{n+\frac{1}{2}}(i, j, k) - F^{n-\frac{1}{2}}(i, j, k)}{\Delta t} + O(\Delta t^2), \quad (5.7)$$

By using the quotients in form (5.6) and (5.7) to replace the differential quotient in Maxwell's vorticity equations, we can gained Yee's differential equations. For example, by applying the central differential quotient approximation to  $E_x$  at point  $\left[i + \frac{1}{2}, j, k\right]$  and time  $\left[n + \frac{1}{2}\right]$ , we can get:

$$\frac{E_x^{n+1}\left(i+\frac{1}{2},j,k\right)-E_x^n\left(i+\frac{1}{2},j,k\right)}{\Delta t} = \frac{1}{\varepsilon\left(i+\frac{1}{2},j,k\right)} \cdot \left[ \frac{H_x^{n+\frac{1}{2}}\left(i+\frac{1}{2},j+\frac{1}{2},k\right)-H_x^{n+\frac{1}{2}}\left(i+\frac{1}{2},j-\frac{1}{2},k\right)}{\Delta y} - \frac{H_x^{n+\frac{1}{2}}\left(i+\frac{1}{2},j,k+\frac{1}{2}\right)-H_x^{n+\frac{1}{2}}\left(i+\frac{1}{2},j,k-\frac{1}{2}\right)}{\Delta z} - \sigma_e \cdot E_x^{n+\frac{1}{2}}\left(i+\frac{1}{2},j,k\right) \right], \quad (5.8)$$

There are 3  $E_x$  values exist in the differential equation (5.8) with a half time step between each others, which result of inconvenience in the real coding and computation. In order to overcome this drawback, we can utilize the following approximation:

$$E_x^{n+\frac{1}{2}}\left(i+\frac{1}{2},j,k\right) = \frac{1}{2} \left[ E_x^{n+1}\left(i+\frac{1}{2},j,k\right) + E_x^n\left(i+\frac{1}{2},j,k\right) \right]$$

As a result, we can obtain the following differential equation about  $E_x$  from equation (5.8):

$$E_x^{n+1}\left(i+\frac{1}{2},j,k\right) = \frac{1-\frac{\sigma_e\left(i+\frac{1}{2},j,k\right)\Delta t}{2\varepsilon\left(i+\frac{1}{2},j,k\right)}}{1+\frac{\sigma_e\left(i+\frac{1}{2},j,k\right)\Delta t}{2\varepsilon\left(i+\frac{1}{2},j,k\right)}} \cdot E_x^n\left(i+\frac{1}{2},j,k\right) + \frac{\Delta t}{\varepsilon\left(i+\frac{1}{2},j,k\right)} \cdot \frac{1}{1+\frac{\sigma_e\left(i+\frac{1}{2},j,k\right)\Delta t}{2\varepsilon\left(i+\frac{1}{2},j,k\right)}} \cdot \left[ \frac{H_x^{n+\frac{1}{2}}\left(i+\frac{1}{2},j+\frac{1}{2},k\right)-H_x^{n+\frac{1}{2}}\left(i+\frac{1}{2},j-\frac{1}{2},k\right)}{\Delta y} - \frac{H_x^{n+\frac{1}{2}}\left(i+\frac{1}{2},j,k+\frac{1}{2}\right)-H_x^{n+\frac{1}{2}}\left(i+\frac{1}{2},j,k-\frac{1}{2}\right)}{\Delta z} \right], \quad (5.9)$$

The differential equations of other electrical field components can be obtained by the same method, and their forms are all similar.

On the other hand, the differential equations of magnetic field components are easy to solve due to the symmetry between equation (5.2) and (5.3). Because of the magnetic field components  $H$  in equation (5.9) are all in  $n + \frac{1}{2}$  time steps, the latter  $H$  values have to be in  $n + \frac{1}{2}$  or  $n - \frac{1}{2}$  time steps, in order to ensure the time step distance between each values is one time step length. For  $H_x$  we have :

$$H_x^{n+\frac{1}{2}}\left(i, j+\frac{1}{2}, k+\frac{1}{2}\right) = \frac{1-\frac{\sigma_m(i, j+\frac{1}{2}, k+\frac{1}{2})\Delta t}{2\mu(i, j+\frac{1}{2}, k+\frac{1}{2})}}{1+\frac{\sigma_m(i, j+\frac{1}{2}, k+\frac{1}{2})\Delta t}{2\mu(i, j+\frac{1}{2}, k+\frac{1}{2})}} \cdot H_x^{n-\frac{1}{2}}\left(i, j+\frac{1}{2}, k+\frac{1}{2}\right) + \frac{\Delta t}{\mu(i, j+\frac{1}{2}, k+\frac{1}{2})} \cdot \frac{1}{1+\frac{\sigma_m(i, j+\frac{1}{2}, k+\frac{1}{2})\Delta t}{2\mu(i, j+\frac{1}{2}, k+\frac{1}{2})}} \cdot \left[ \frac{E_y^n(i, j+\frac{1}{2}, k+1) - E_y^n(i, j+\frac{1}{2}, k)}{\Delta z} - \frac{E_z^n(i, j+1, k+\frac{1}{2}) - E_z^n(i, j, k+\frac{1}{2})}{\Delta y} \right], \quad (5.10)$$

Similar equations for  $H_y$  and  $H_z$  can be obtained by same method.

From equations (5.9) and (5.10) we can find, this algorithm has one significant feature that for any grid points, its electrical components are only related to the value itself at the previous time step and the magnetic components around it; similarly, its magnetic components are only related to itself at the previous time step and the electrical components around it. Also, the parameters  $\varepsilon$ ,  $\mu$ ,  $\sigma_e$ , and  $\sigma_m$  are all expressed as functions of spatial coordinate. This means these parameters can be set to be nonuniform and anisotropic. Therefore, this algorithm is effective and convenient while dealing with medium with nonuniformity and anisotropy.

Equations (5.9) and (5.10) are the general form while the spatial grid sizes of lattice  $\Delta x$ ,  $\Delta y$ , and  $\Delta z$  have different values. However, when there are no specific requirements, it is usually to set a same value for the three spatial grid sizes, and the lattice is going to become cubic. Let's use  $\Delta s$  to express the unified spatial grid size, then we have

$$\Delta s = \Delta x = \Delta y = \Delta z$$

Then the coefficients in equations (5.9) and (5.10) can be simplified as following:

$$CA(i, j, k) = \frac{1-\frac{\sigma_e(i, j, k)\Delta t}{2\varepsilon(i, j, k)}}{1+\frac{\sigma_e(i, j, k)\Delta t}{2\varepsilon(i, j, k)}}, \quad (5.11a)$$

$$CB(i, j, k) = \frac{\Delta t}{\varepsilon(i, j, k)\Delta s} \cdot \frac{1}{1+\frac{\sigma_e(i, j, k)\Delta t}{2\varepsilon(i, j, k)}}, \quad (5.11b)$$



$$DA(i, j, k) = \frac{1 - \frac{\sigma_m(i, j, k)\Delta t}{2\mu(i, j, k)}}{1 + \frac{\sigma_m(i, j, k)\Delta t}{2\mu(i, j, k)}} \quad (5.12a)$$

$$DB(i, j, k) = \frac{\Delta t}{\mu(i, j, k)\Delta s} \cdot \frac{1}{1 + \frac{\sigma_m(i, j, k)\Delta t}{2\mu(i, j, k)}} \quad (5.12b)$$

The  $(i, j, k)$  here is to indicate that these parameters are generally functions of the spatial coordinate. Even in the same grid, due to the half grid size resolution, they can be with a different number of  $(i, j, k)$ , to express the nonuniformity and anisotropy of the medium. After using the simplified signs above, equations (5.9) and (5.10) can be transformed to:

$$E_x^{n+1}\left(i + \frac{1}{2}, j, k\right) = CA\left(i + \frac{1}{2}, j, k\right) \cdot E_x^n\left(i + \frac{1}{2}, j, k\right) + CB\left(i + \frac{1}{2}, j, k\right) \cdot \left[ H_x^{n+\frac{1}{2}}\left(i + \frac{1}{2}, j + \frac{1}{2}, k\right) - H_x^{n+\frac{1}{2}}\left(i + \frac{1}{2}, j - \frac{1}{2}, k\right) + H_x^{n+\frac{1}{2}}\left(i + \frac{1}{2}, j, k - \frac{1}{2}\right) - H_x^{n+\frac{1}{2}}\left(i + \frac{1}{2}, j, k + \frac{1}{2}\right) \right], \quad (5.13)$$

$$H_x^{n+\frac{1}{2}}\left(i, j + \frac{1}{2}, k + \frac{1}{2}\right) = DA\left(i, j + \frac{1}{2}, k + \frac{1}{2}\right) \cdot H_x^{n-\frac{1}{2}}\left(i, j + \frac{1}{2}, k + \frac{1}{2}\right) + DB\left(i, j + \frac{1}{2}, k + \frac{1}{2}\right) \cdot \left[ E_y^n\left(i, j + \frac{1}{2}, k + 1\right) - E_y^n\left(i, j + \frac{1}{2}, k\right) + E_z^n\left(i, j, k + \frac{1}{2}\right) - E_z^n\left(i, j + 1, k + \frac{1}{2}\right) \right], \quad (5.14)$$

It can be observed from equations (5.13) and (5.14) that, if there are  $N$  grids in the whole computation region, then data required for storage includes six EM field components and four medium parameters, and their amount are all  $N$ . Despite the existence of EM field components at the two adjacent time steps, the algorithm requires to store only the results for one of them because there's no repeated using. As a result, the required storage space of FDTD method is positively proportional to  $N$ , and thus the CPU time needed for FDTD method is also positive proportional to  $N$ . This feature is very valuable, especially when  $N$  is pretty large. Also, if we assume that the medium in computation region is distributed in areas uniformly, the expression of medium parameters can be further simplified, and hence further reduce the required storage space, the number of required practical storage units for medium parameters

is equal to the number of areas.

Another feature of FDTD method can be summarized from the differential equations. It is not like those vector methods and frequency domain methods which ultimately result to solve an algebraic equations group, but to calculate the field components at each time step directly from itself at previous time step and adjacent field components.

Note that in most of the EM field problems, there's no magnetic medium in computation region, in this condition, we have  $\mu = \mu_0$ , and  $\sigma_m = 0$ . In addition, some of the problems can be simplified to 2-dimension, the equations in this condition can be gained from the 3-dimensional equations by neglecting  $z$  components.

In the simulation software used for this thesis, the directions are set to be as following:  $x$  is vertical upwards,  $z$  is horizontal to the right, and  $y$  is perpendicular to the screen towards us, therefore when calculating in 2-dimensions, the neglected components are  $y$  components.

There are much more details in the basic theory of FDTD method in electromagnetism. However, this thesis is just based on FDTD simulation, but not in the topic of FDTD theory, so the rest part of the theory is not going to be introduced here.

In this thesis, all the results are simulated by utilizing a commercial software called "OmniSim" from the Photon Design Company.

## CONCLUSION

This thesis introduced the three main research projects completed by the author, with background introduction of integrated ring resonator and Finite Difference Time Domain (FDTD) method in electromagnetism. The conclusion for each project is summarized at the end of each chapter. As the overall conclusion, here a summary of the entire thesis is stated. The particle position sensor in chapter two is proposed with two designs, to suit the condition with or without a high-resolution spectrometer. The hydrogen sensor proposed in Chapter three gives a solution to detect hydrogen with fast response, ultra small size and the possibility to be integrated with other components. The results in Chapter four indicate the failure in designing an easily fabricated wideband reflector in visible range based on HCG subwavelength grating structure. However, the results are still valuable for further study.

## REFERENCES

- [1] T. Huberta, L. Boon-Brettb, G.Blackb, U. Banacha, "Hydrogen sensors – A review," *Sensors and Actuators B: Chemical*, vol.157, pp.329-352, Oct. 2011
- [2] Minghong Yang, Jixiang Dai, "Fiber Optic Hydrogen Sensors: a Review", *Photonic Sensors*, Volume 4, Issue 4, pp 300-324, Dec 2014
- [3] G. Jonsson, L. Gorton, "An electrochemical sensor for hydrogen peroxide based on peroxidase adsorbed on a spectrographic graphite electrode," *Anal. Chim. Acta*, vol.1, pp.465-468, Sep. 1989
- [4] F. Favier, E. C. Walter, M. P. Zach, T. Benter, T. R. M. Penner, "Hydrogen sensors and switches from electrodeposited palladium mesowire arrays," *Science*, vol. 293, pp.2227-2231, Sep. 2001
- [5] Y. Lu, J. Li, J. Han, H.T. Ng, C. Binder, C. Partridge, M. Meyyappan, "Room temperature methane detection using palladium loaded single-walled carbon nanotube sensors," *Chem. Phys. Lett.*, vol. 391, pp.344-348, Jun. 2004
- [6] F. Song, A. L. Garner, and K. Koide, "A Highly Sensitive Fluorescent Sensor for Palladium Based on the Allylic Oxidative Insertion Mechanism," *J. Am. Chem. Soc.*, vol. 129, pp.12354-12355, Sep. 2007
- [7] B.P. Luther, S.D. Wolter, S.E. Mohney, "High temperature Pt Schottky diode gas sensors on n-type GaN," *Sens. Actu. B: Chem.*, vol. 56, pp.164-168, Jul, 1999
- [8] L. Wang, E. Wang, "A novel hydrogen peroxide sensor based on horseradish peroxidase immobilized on colloidal Au modified ITO electrode," *Elec. Comm.*, vol. 6, pp. 225-229, Feb, 2004
- [9] F. D. Jr, I. S. Chen, P. Chen, J. Neuner, A. Roerhla, J. Welcha, "MEMS-based hydrogen gas sensors," *Sens. Actu. B: Chem.*, vol. 117, pp.10-16, Sep, 2006
- [10] A. Haddadpour and Y. Yi, "Metallic nanoparticle on micro ring resonator for bio optical detection and sensing," *Biomedical Optics Express*, vol. 1, pp.378-384, Sep. 2010
- [11] M. Ostrowski, P. Pignalosa and Y. Yi, "Higher order optical resonance node detection of integrated disk micro resonator," *Opt. Lett.*, vol. 36, pp.3042-3044, Aug. 2011
- [12] E. Krioukov, D. J. W. Klunder, A. Driessen, J. Greve, and C. Otto, "Sensor based on an integrated optical microcavity," *Opt. Lett.* vol. 27, pp.512-514, Apr. 2002
- [13] L. Goddard, K. Y. Wong, A. Garg, E. Behymer, G. Cole, and T. Bond, "Measurements of

the complex refractive index of Pd and Pt films in air and upon adsorption of H<sub>2</sub> gas,” *Proceedings of IEEE CLEO/LEOS 2008*

[14] A. Hessel and A. A. Oliner, “A new theory of Wood’s anomalies on optical gratings,” *Appl. Opt.*, vol. 4, no. 10, pp. 1275–1297, Oct. 1965.

[15] S. S. Wang, R. Magnusson, J. S. Bagby, and M. G. Moharam, “Guided-mode resonances in planar dielectric-layer diffraction gratings,” *J. Opt. Soc. Amer. A*, vol. 7, no. 8, pp. 1470–1474, Aug. 1990.

[16] C. J. Chang-Hasnain and W. Yang, “High-contrast gratings for integrated optoelectronics,” *Adv. Opt. Photon.*, vol. 4, no. 3, pp. 379–440, Sep. 2012.

[17] C. F. R. Mateus, M. C. Y. Huang, Y. Deng, A. R. Neureuther, and C. J. Chang-Hasnain, “Ultrabroadband mirror using low-index cladded subwavelength grating,” *IEEE Photon. Technol. Lett.*, vol. 16, no. 2, pp. 518–520, Feb. 2004.

[18] Z. S. Liu, S. Tibuleac, D. Shin, P. P. Young, and R. Magnusson, “High- efficiency guided-mode resonance filter,” *Opt. Lett.*, vol. 23, no. 19, pp. 1556–1558, Oct. 1998.

[19] A. Szeghalmi, E. B. Kley, and M. Knez, “Theoretical and experimental analysis of the sensitivity of guided mode resonance sensors,” *J. Phys. Chem. C*, vol. 114, no. 49, pp. 21150–21157, Dec. 2010.

[20] S. F. Lin et al., “A model for fast predicting and optimizing the sensitivity of surface-relief guided mode resonance sensors,” *Sens. Actuators B, Chem.*, vol. 176, no. 1, pp. 1197–1203, Jan. 2013.

[21] A. Y. Zhu, S. Zhu, and G.-Q. Lo, “Guided mode resonance enabled ultra-compact germanium photodetector for 1.55  $\mu\text{m}$  detection,” *Opt. Exp.*, vol. 22, no. 3, pp. 2247–2258, Feb. 2014.

[22] Y.-R. Lin, K. Y. Lai, H.-P. Wang, and J.-H. He, “Slope-tunable Si nanorod arrays with enhanced antireflection and self-cleaning properties,” *Nanoscale*, vol. 2, no. 12, pp. 2765–2768, Dec. 2010.

[23] Y. Wang et al., “Biomimetic corrugated silicon nanocone arrays for self-cleaning antireflection coatings,” *Nano Res.*, vol. 3, no. 7, pp. 520–527, Jul. 2010.

[24] K. B. Crozier, A. Sundaramurthy, G. S. Kino, and C. F. Quate, “Optical antennas: Resonators for local field enhancement,” *J. Appl. Phys.*, vol. 94, no. 7, pp. 4632–4642, Oct. 2003.

[25] A. V. Kabashin et al., “Plasmonic nanorod metamaterials for biosensing,” *Nature Mater.*, vol. 8, no. 11, pp. 867–871, Oct. 2009.

[26] R. Magnusson, “Wideband reflectors with zero-contrast gratings,” *Opt. Lett.* 39, 4337 (2014).

- [27]S. Wang, K. Broderick, H. Smith, and Y. Yi, “Strong coupling between on chip notched ring resonator and nanoparticle”, *Applied Phys. Letter*, Vol. 97, pp 051102\_1-051102\_3, Aug 2010
- [28]Ostrowski M, Pignalosa P, Smith H, Yi Y, “Higher-order optical resonance node detection of integrated disk microresonator”, *Optics letters*, vol. 36(16), pp. 3042-3044, Aug. 2011
- [29]Betzig EJ, Trautman JK, Harris TD, Weiner JS, “Kostelak RL. Breaking the diffraction barrier- optical microscopy on a nanometric scale”, *Science*, 251(5000), pp. 1468-1470, Mar 1991
- [30]Suzuki, Senichi, Kazuhiro Oda, and Yoshinori Hibino, “Integrated-optic double-ring resonators with a wide free spectral range of 100 GHz”, *Journal of lightwave Tech.*, vol. 13(8), pp. 1766-1771, Aug. 1995
- [31]Lee, Mindy R., and Philippe M. Fauchet, “Nanoscale microcavity sensor for single particle detection”, vol. 32, no. 22, pp.3284-3286, Nov. 2007
- [32]Ostrowski M, Pignalosa P, Smith H, Yi Y, “Higher-order optical resonance node detection of integrated disk microresonator”, *Optics letters*, vol. 36(16), pp. 3042-3044, Aug. 2011
- [33]Nie, Shuming, and Steven R. Emory, “Probing single molecules and single nanoparticles by surface-enhanced Raman scattering”, *Science*, vol. 275(5303), pp. 1102-1106, Mar. 1997
- [34]Va, C., Julio Montalvo, and Pedro C. Lallana, “Radio-frequency ring resonators for self-referencing fiber-optic intensity sensors”, *Optical Engineering*, vol. 44(4), pp. 040502\_1-040502\_2, Apr. 2005
- [35]Heijne, E.H., Jarron, P., Olsen, A. and Redaelli, N., “The silicon micropattern detector: a dream?”, *Nuclear Instruments and Methods in Physics Research Section A: Accelerators, Spectrometers, Detectors and Associated Equipment*, vol. 273(2), pp.615-619, Dec. 1988
- [36]Rafizadeh D, Zhang JP, Hagness SC, Taflove A, Stair KA, Ho ST, Tiberio RC, “Waveguide-coupled AlGaAs/GaAs microcavity ring and disk resonators with high finesse and 21.6-nm free spectral range”, *Optics Letters*, vol. 22(16), pp. 1244-1246, Aug. 1997
- [37]Zhu, J., Ozdemir, S.K., Xiao, Y.F., Li, L., He, L., Chen, D.R. and Yang, L., “On-chip single nanoparticle detection and sizing by mode splitting in an ultrahigh-Q microresonator”, *Nature Photonics*, vol. 4(1), pp.46-49, Dec. 2009
- [38]Li, Ming, Xiang Wu, Liying Liu, Xudong Fan, and Lei Xu., “Self-referencing optofluidic ring resonator sensor for highly sensitive biomolecular detection”, *Analytical chemistry*, vol. 85(19), pp. 9328-9332, Aug. 2013
- [39] T. Claes, W. Bogaerts, and P. Bienstman, " Experimental characterization of a silicon photonic biosensor consisting of two cascaded ring resonators based on the Vernier-effect and introduction of a curve fitting method for an improved detection limit", *Opt. Express* 18,

22747, 2010.

[40] P. R. Prasad, S. K. Selvaraja, and M. M. Varma, "Thermo-optical tuning of cascaded double micro-ring resonators for dynamic range enhancement", Proc. SPIE 9725, 97250O, 2016.

[41] P. R. Prasad, S. K. Selvaraja, and M. M. Varma, " High precision measurement of intensity peak shifts in tunable cascaded microring intensity sensors", *Optics Letters*, Vol. 41, No. 14, July 2016.

[42] L. Jin, M. Li, and J.-J. He, in Asia Communications and Photonics Conference, Technical Digest, OSA Technical Digest Series (Optical Society of America, 2009), paper TuM4.

[43] L. Jin, M. Li, and J.-J. He, in Conference on Lasers and Electro-Optics, OSA Technical Digest Series (Optical Society of America, 2010), paper JWA84.

[44] L. Jin, M. Li, and J.-J. He, *Opt. Commun.* 284, 156 (2011).

[45] D. Dai, *Opt. Express* 17, 23817 (2009).

[46] L. Jin, M. Li, and J.-J. He, *Opt. Lett.* 36, 1128 (2011).

[47] L. Jin, M. Li, and J.-J. He, *J. Lightwave Technol.* 30, 1994, (2012).

[48] D. Rabus, *Integrated Ring Resonators-The Compendium* (Springer, 2007).

[49] Yin Xu, Xumin Gao, Dan Bai, Xin Li, Yongjin Wang, " WIDEBAND REFLECTORS FASHIONED WITH FREESTANDING HFO<sub>2</sub> RESONANT GRATINGS", 2015 14th International Conference on Optical Communications and Networks (ICOON)

## PUBLICATIONS

### Conference:

- [1] D. Wu, W. Yu, X. Duan and Y. Yi, 'Sub-wavelength grating structure with high aspect ratio and tapered sidewall', *MRS Advances*, 1, 32 (2016)
- [2] W. Yu, D. Wu, X. Duan and Y. Yi, 'Sub-wavelength grating wide band reflectors with tapered sidewall', *MRS Advances*, 1, 18 (2016)

### Journal:

- [1] Y. Yi, P. Pignalosa, and D. Wu, 'Tunable and ultra-small graphene integrated silicon racetrack micro resonator', *IEEE Journal of Selected Topics in Quantum Electronics*, VOL. 23, NO. 1, 8200306 (2017)
- [2] Y. Yi, D. Wu, P. Birar, and Z. Yang, 'Ring resonator based optical hydrogen sensor', *IEEE Sensors Journal*, 17, 2042 (2017)
- [3] Y. Yi and D. Wu, 'Plasmonic hydrogen sensor based on integrated micro ring resonator', *Optical Engineering*, 56, 121904 (2017)